2018

In-situ stress monitoring during corrosion and electrodeposition

Brendan Shin Hau Yeah
Iowa State University

In-situ stress monitoring during corrosion and electrodeposition

by

Brendan Shin Hau Yeah

A thesis submitted to the graduate faculty

in partial fulfillment of the requirements for the degree of

MASTER OF SCIENCE

Major: Mechanical Engineering

Program of Study Committee:
Pranav Shrotriya, Major Professor
Kurt Hebert
Sonal Padalkar

The student author, whose presentation of the scholarship herein was approved by the program of study committee, is solely responsible for the content of this thesis. The Graduate College will ensure this thesis is globally accessible and will not permit alterations after a degree is conferred.

Iowa State University

Ames, Iowa

2018

TABLE OF CONTENTS

Page

LIST OF FIGURES

Page

LIST OF TABLES

Page

ACKNOWLEDGMENTS

I would like to thank my major professor, Dr. Pranav Shrotriya, for his patient guidance and help throughout my master's study. I would not be able to achieve and accomplish the works without his continuous supervision.

I would like to express my gratitude and appreciation to my fellow committee members, Dr. Kurt Hebert and Dr. Sonal Padalkar for serving as my Program of Study and Committee (POSC) and their valuable inputs and suggestions throughout the research projects.

In addition, I would like to thank my fellow mentors, collaborators and current and ex-members from our research group, Abdullah Alshehri, Agnivo Gosai, Zhichen Zhu, Kwang Shiong Wong, Ibraheem Redhwi, Faez Qahtani, Sivaranjani Devarakonda and Tian Lan for the continuous guidance and discussions towards my research projects. I know I always can count on them whenever I need help from them.

Lastly, I would like to thank my family and friends for the unconditional love and support throughout my graduate school life. Without them, I would not be able to be who I am today!

ABSTRACT

High strength aluminum alloys of 2XXX and 5XXX series are widely utilized in recent years for marine, transportation and structural applications, due to low cost, high strength–to-weight ratio as well as good corrosion resistance. However, the aluminum alloys are susceptible to Intergranular Corrosion (IGC) or Intergranular attack (IGA), a form of metal degradation along the selective grain boundary element in a corrosive environment. For instance, Al-Cu-Mg alloy, AA2024-T3 is vulnerable to IGC with the dissolution of S phase, Al_2CuMg particles that precipitate along the grain boundaries. Similarly, Al-Mg alloy, AA5083 is susceptible to IGC with the precipitation of β phase, Mg_2Al_3 particles along the grain boundaries of the alloy when exposed to long term elevated temperature (60 ˚C ~ 180 ˚C).

In the present work, we utilized in-situ stress measurement during IGC of 2024 and 5083 to determine the mechanism relating corrosion induced stress fields and grain boundary dissolution. Phase shifting curvature interferometer, a method proven to be effectively detects electrochemical reaction induced curvature changes which is utilized to monitor the sample curvature during IGC. AA2024-T3 and sensitized AA5083-H116 samples were cut and polished then mounted in electrochemical cell with the front surface exposed to solution (aqueous 1 M NaCl for AA2024-T3, aqueous 3.5 wt% NaCl for sensitized AA5083-H116) and the mirror polished back surface utilized for in situ stress measurements. The electrochemical tests were performed with a three-electrode setup. Anodic potentiodynamic polarization was performed at a rate of 0.167 mV/s starting from -0.9 V to -0.3 V followed by a 30-minute open circuit potential (OCP). Subsequently, the samples were held at 0.1 V above the OCP value (-0.535 V for

AA2024 samples and -0.63 V for sensitized AA5083) to monitor stress development during anodic dissolution. Corrosion surface morphology was examined with Scanning Electron Microscopy (SEM) and Energy-Dispersive Spectrometer (EDS).

Experimental results show that anodic dissolution of both 2024 and 5083 are associated with development of compressive stresses in the sample surfaces. The compressive stresses development is at low magnitude during open circuit exposure and stepping to the higher potential results in large dissolution current and rapid development of compressive stresses. Microstructural and compositional characterization of the sample surfaces show evidence of grain boundary dissolution and formation of pits. The grain boundaries show higher concentration of oxygen indication formation of oxides during the anodic dissolution. The observation of compressive stress generation during anodic dissolution and presence oxides at grain boundaries indicates that dissolution of intermetallic particles segregated at the grain boundary results in formation of oxides. The volume increase associated with oxide formation acts as wedges in the grain boundary resulting in compressive stresses on the sample surface. The oxide formation induced wedging stresses may contribute to intergranular stress corrosion cracking of these alloys.

Cuprous Oxide or Copper (I) Oxide (Cu_2O), a p-type semiconductor is a promising candidate for various applications such as photocatalyst for solar driven water splitting of and H_2 generation, electrode for lithium ion batteries and p-type semiconductor in heterojunction with n-type ZnO for photovoltaic applications. The Cu_2O has a direct bandgap of 2.17eV that is able to absorb major portion of the visible light spectrum which favours the PEC hydrogen production. According to Shockley-

Queisser limit graph, Cu_2O with a direct band gap of 2.0–2.2 eV, which has an approximate maximum efficiency of 18%. Moreover, Cu_2O is low cost, abundantly available in nature and easily produced via electrodeposition and sputtering where the production methods are simple, economical and scalable.

A new phase shifting curvature interferometry, a technique used for high-resolution in-situ stress measurement of electrochemical reactions. The curvature changes that could be resolved by curvature interferometry system is as small as 1×10^{-4} m^{-1}. It was demonstrated that small curvature change rates of 2.5×10^{-8} $m^{-1}s^{-1}$ could also be reliably measured, indicating the applicability of the system to measure bulk samples. In the present work, the phase shifting curvature interferometry is utilized to measure the deflection and stress development on the Indium Tin Oxide-Au (ITO-Au) sample during electrodeposition of Cu_2O. Experimental results show that electrodeposition of Cu_2O are associated with the compressive stress development in the sample surface. The Au-Cu_2O interface layer exerted high stress on the sample due to mismatch of lattice between the Au and Cu_2O while the remaining Cu_2O deposited layers are in stress free zone.

CHAPTER 1. INTRODUCTION

1.1 Corrosion

1.1.1 Introduction to Corrosion

Corrosion is natural phenomena that is defined as the deterioration of metal by forming an oxide layer on the surface due to environment effect according to Snow et al., 2001 [42] and The Electrochemical Society (ECS) [www.electrochem.org]. The deeper understanding towards corrosion is the electrochemical oxidation process with an oxidant, commonly is oxygen. In general, corrosion process not only seen in metals but also can also be found in all other types of materials ranging from glasses, ceramics and polymers. The conditions that could drive the deterioration of metals include presents of water molecules, immersion in electrolyte, pH value of electrolyte, lacks protective layer on material surface and experiences of defects or loaded stress on material surface.

The reddish-brown coloration found on surface of material is the rust formation on metal surface due to the formation of oxides or salts from the material matrix body. The formation of rust on the surface of material can be found in various applications such as transportation, pipelines and structural components. Figure 1.1 illustrated the example of the chemical reaction of rust formation on the surface of pipeline made from iron due to the presence of electrolyte and accordingly moist environment such as coastal area that would drives the formation of rust faster than dry environment. The iron body acts as anode, where oxidation occurs (loss of electrons), the electrons migrate to cathode via an electrical connection. Oxygen gas from the atmosphere acts as cathode, where reduction occurs (gain of electrons), the electrons receive from anode. Water functioned as “salt bridge” in the galvanic cell setup

to allow metal ions to transfer from one side of the solution. The half-cell reaction of the chemical reaction can be written as:

Anode half reaction:

$$Fe_s \rightarrow Fe^{2+}{}_{aq} + 2e^-$$

Cathode half reaction:

$$O_{2_g} + 2H_2O_l + 4e^- \rightarrow 4OH^-{}_{aq} \quad (1.2)$$

Overall reaction:

$$2Fe_s + O_{2_g} + 2H_2O_l \rightarrow 2Fe^{2+}{}_{aq} + 4OH^-{}_{aq} \quad (1.3)$$

General Rust Formation:

$$Fe^{2+}{}_{aq} + 2OH^-{}_{aq} \rightarrow Fe(OH)_{2_s} \quad (1.4)$$

$$Fe(OH)_{2_s} + O_{2_g} + xH_2O_l \rightarrow 2Fe_2O_3 \cdot (x+4)H_2O_s \quad (1.5)$$

Iron (Fe) is oxidized into ferrous (Fe^{2+}) ions at anodic site where Fe^{2+}enter the electrolyte. The electrons released from Fe transferred to cathodic site via conductive material that connects anode and cathode. *Oxygen gas (O_2) is reduced to water at the cathodic site on the surface of the iron.* The Fe^{2+} in the electrolyte oxidized with hydroxide ions (OH^-) to form iron (II) hydroxide ($Fe(OH)_2$). $Fe(OH)_2$ is further oxidized react with O_2 and water (H_2O) to form hydrated iron (III) oxide ($2Fe_2O_3 \cdot xH_2O$) commonly known as rust.

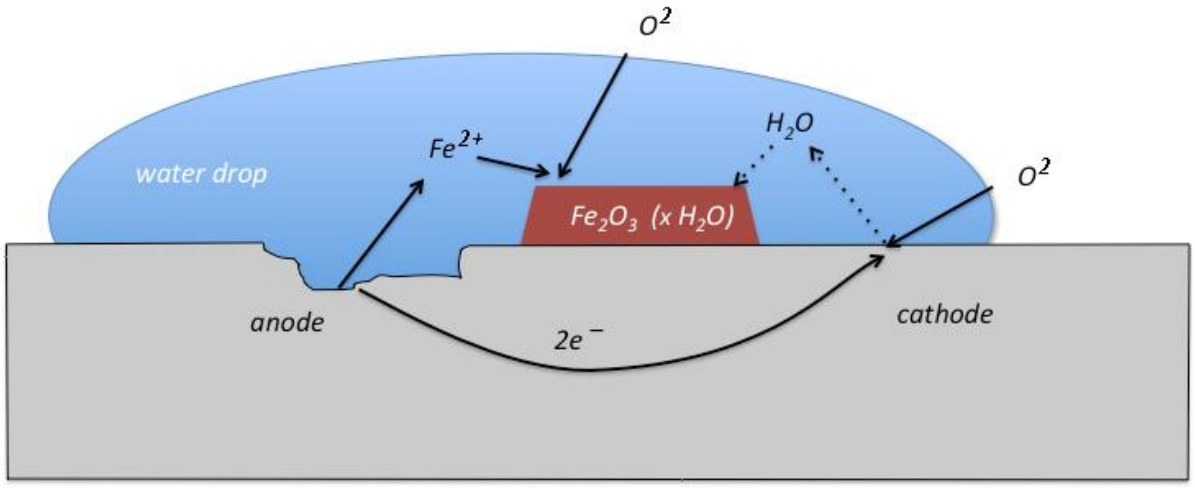

Figure 1.1 Complete chemical reaction illustration for the rust formation of the surface of iron. [1, 2]

1.1.2 Forms of corrosion

Corrosion can occur in various forms and the main forms are uniform surface corrosion, galvanic corrosion, pitting corrosion, intergranular corrosion (IGC) and stress corrosion cracking (SCC).

1.1.2.1 Uniform Surface Corrosion

Uniform or general surface corrosion is the most common form of corrosion cause by an electrochemical reaction that occur over the surface area of metal when exposed to corrosive environment. Figure 1.2 depicted the uniform surface corrosion occurred over the surface of metal where a layer of oxide or salt are formed in the process.

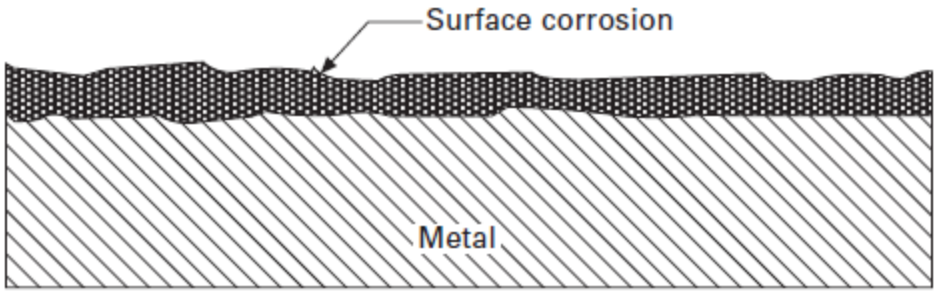

Figure 1.2 Schematic representation of uniform surface corrosion across the surface of metal [4]

1.1.2.2 Galvanic Corrosion

Galvanic corrosion occurs when two different metals are connected in an electrolyte, one metal will experience an accelerated corrosion process while the other metal will be protected from the corrosion process. The potential difference between the two different metals produces an electron flow from anode to cathode. The electrode at cathode experience reduction where the electrode receives electrons to form protective layer while the electrode at anode experience oxidation where electrode loss electrons. Figure 1.3 illustrated the example of the metals that are more reactive and noble to one another. The further the two metals apart in the chart, the vigorous the corrosion process for the less noble metal.

Figure 1.3 Galvanic series chart for various metals with top lists representing more active metals and bottom list representing more noble metals. [3]

1.1.2.3 Pitting Corrosion

Pitting is the localized dissolution of metal due to the breakdown of natural formed passive film on metal surface such as stainless steel and aluminium alloys [13-15]. The accelerated localized attack on the passivated films on metal surface will form small holes and cavities that resulted by site galvanic reaction when exposed to electrolyte. Figure 1.4 illustrated aggressive anion penetrated and attacked the passive films thus forming pits on the surface while the large area of the material remains unattacked.

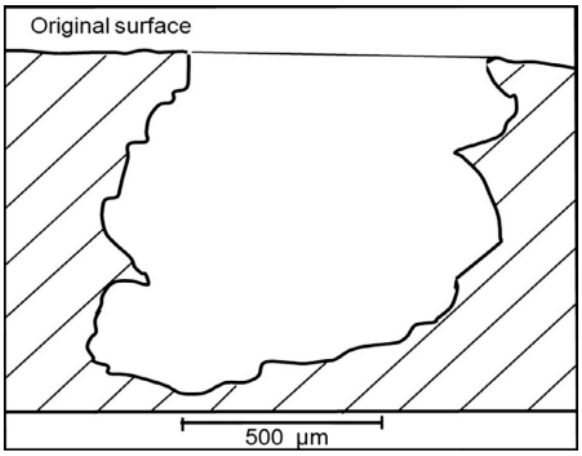

Figure 1.4 Schematic illustrated the pitting corrosion where localized attack penetrated deep into the material body forming small pits [4].

1.1.2.4 Intergranular corrosion (IGC)

IGC is the preferential localized attack along the grain boundary of metals due to the chemical segregation effect or precipitation of secondary phase particles along the grain boundaries. The dissolution process of materials tends to propagate along intergranular pathways due to the chemical composition difference between the material in the matrix body and grain boundary as shown in figure 1.5(a). Similarly, to the galvanic cell mentioned above, the presence of electrolyte provided a connection between the grain boundary and matrix body. IGC commonly studied metal alloys such as 2xxx and 5xxx series aluminium alloys [5-9] and stainless steel [10-12]

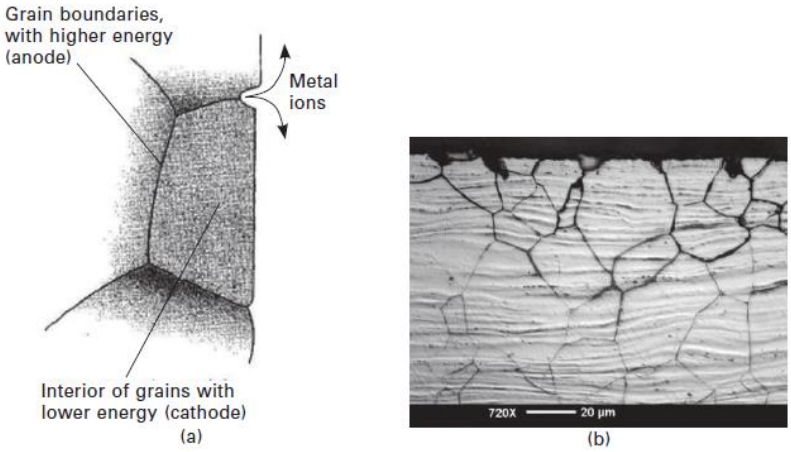

Figure 1.5 (a) Schematic of intergranular corrosion along the grain boundary (b) Image of intergranular corrosion along the grain boundary under the material surface [4].

1.1.2.5 Stress Corrosion Cracking (SCC)

SCC is a form of corrosion induced by the combination of three key factors which are stress, susceptible material and specific corrodent. External applied stress from load and internal applied stress from metal manufacturing process are both source that lead to stress acting on material [4]. T.D. Burleigh summarized three mechanisms that induced SCC which are active path, hydrogen embrittlement and brittle film induced cleavage [16]. Active path refers to the crack propagation due to the metal dissolution and tensile forces at crack tip, similarly to IGC if the metal dissolution favors the grain boundaries. Hydrogen embrittlement refers to brittle areas at crack tip location caused by high hydrogen concentration under tensile loading. Cleavages are formed when cracks are formed and propagated on the surface of the metal which is induced by brittle film. SCC is responsible for the fracture and rupture of various metal alloys and the most common application is underground steel pipelines [17-22]. SCC can starts with pits and propagates deeper into the material body along the grain boundaries as shown in figure 1.6.

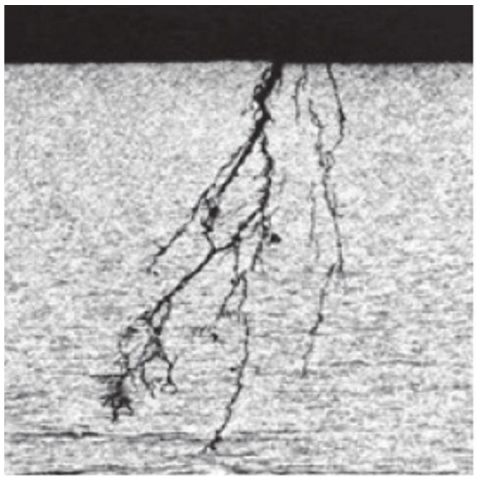

Figure 1.6 Subsurface view image of Stress Corrosion Cracking (SCC) that propagates deeper into the body starting from the material surface [4].

1.1.3 Introduction to Aluminium Alloys

Rust normally only refers to the corrosion of iron and steel while aluminium corrosion is referred as the formation of passive layer, aluminium oxide (Al_2O_3). Aluminium oxide is a thin dense layer of material that prevents the aluminium from further corrosion unlike iron or steel oxides. The formulations below describe how aluminium is oxidised to form aluminium oxide:

$$2Al + 3H_2O \rightarrow Al_2O_3 + 6H^+ + 6e^- \quad (1.6)$$

Al is aluminum in solid state, $H_2O$is water molecule in liquid state, $Al_2O_3$is aluminium oxide in solid state, $H^+$is hydrogen ion and $e^-$is electron. Aluminium alloys have been utilized in various industries ranging from transportation, structural and marine with the desirable mechanical properties provided by the additional of alloying elements. The second phase (intermetallic particles) exbibit an electrochemical characteristic that is differ from the matrix to enhance the corrosion resistance. However, the aluminium alloys are susceptible to different forms of corrosion that can develop into catastrophic failure. In Chapter 2, detail

information about the forms of corrosion of aluminium 2xxx and 5xxx series were mentioned and explained.

1.2 Stress measurement during electrochemical testing

Stress generation in thin film could be monitored during electrodeposition, anodization, etching and dissolution of film. Intrinsic stress is one of the two stresses observed in thin films. The thin film formed on the substrate surface becomes stressed as the thin film and substrate are elastic incompatible [23-25]. The experimental approach to measure stress development in a thin film is using substrate curvature monitoring method. Stoney's thin film stress equation can be utilized to understand the relationship between the stress development in the thin film bonded to the substrate and the curvature of the substrate as shown in equation 1.7 [26].

$$dF = \frac{E_S h_S}{6(1-v)} d\kappa \quad (1.7)$$

dF refers to the in-plane force per unit width change in the film, E_s refers to Young's modulus of elasticity of the substrate, h_s is the substrate thickness, v is the Poisson's ratio of the substrate and dκ is the substrate curvature change. Stoney's equation is used to directly convert the measured curvature change on the substrate into stress generated in thin film on substrate surface. The assumptions for using Stoney's Thin Film Stress Equation to measure curvature change on the substrate surface according to Feng and et al are [33]:

1. Both substrate and coating thickness is very small compared to lateral dimensions
2. Ratio of thin film to substrate thickness is small
3. Edge effect near the peripheral of the substrate is negligible
4. Substrate material is isotropic, homogeneous and linearly elastic
5. Strain and rotations is infinitesimal

Curvature interferometry technique has been utilized to monitor the distribution of stress along the thickness of the substrate with the recorded curvature measurement during experiment. According to Wang and et.al, the curvature interferometry method has proven to reduce the influence of environment and small tilt, vibration or translation of the sample does not have any effect on curvature measurement (28). The high stability and resolution of the curvature interferometry with Curvature changes as small as 10^{-3} km^{-1} were detected and small curvature change rates of 10^{-3} $km^{-1}s^{-1}$ could also be reliably measured for anodizing experiment has been reported by Çapraz and et.al [29]. They reported the in-situ stress measurement using phase-shifting curvature interferometry during aluminum anodizing experiments. The phase-shifting curvature interferometry provides unambiguous path length measurement and eliminates phase-dependent sensitivity. The in-situ stress measurement during anodizing experiment recorded the stress in the oxide was tensile at low current density, slowly developed into compressive at higher current density which correlates the stress results measured from multiple beam deflectrometry by Van Overmeere and et. Al [30]. However, the limitation of the curvature interferometer is the instrument measures the average curvature of the sample. The curvature interferometer technique had been successfully utilized in several other experiments to monitor in-situ stress measurement during anodizing [31-34] and corrosion [35, 36] are also available. The details about theory of phase-shifting curvature interferometry will be discussed in the photoelectrochemical water splitting section.

1.3 Photoelectrochemical Water Splitting

The conversion from solar energy into chemical fuel has been an interesting research topic due to the impact of fossil fuel to the environment. Figure 1.7 illustrated the possibility

of future energy infrastructure based on sunlight, electricity and hydrogen. One of the pathways to achieve conversion of water and sunlight into hydrogen is through phtoelectrochemical (PEC) water splitting with a semiconductor or photoanode.

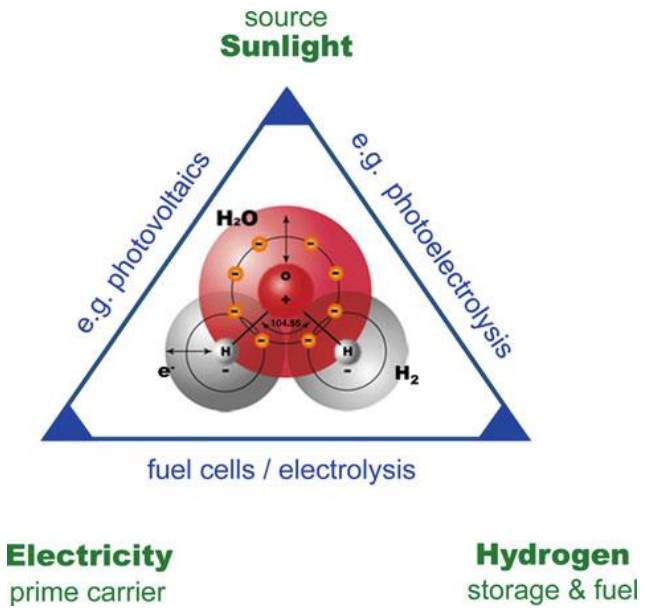

Figure 1.7. Triangle of possible future energy infrastructure [37].

According to Van de Krol, the advantages of photoelectrochemical water splitting are as follows:

a) Hydrogen and oxygen gas are produced at different electrodes and prevented any safety risks.
b) Electrochemical process can be taken place at room temperature without limitation to sunny regions of the world
c) Inorganic material can be utilized as major cell building material with higher durability compared to organic material

The schematic diagram in figure 1.8 illustrated the fundamentals of the PEC water splitting reaction with semiconductor as the working electrode (WE) and metal as the counter

electrode (CE). The semiconductor is responsible to convert incident photons to electron-hole pairs. The electrons (e^-) and holes (h^+) generated by semiconductor are separated by the presence of an electric field inside the semiconductor. The electrons traveled towards the metal surface through an electrical connection between semiconductor and metal to carry out the reduction.

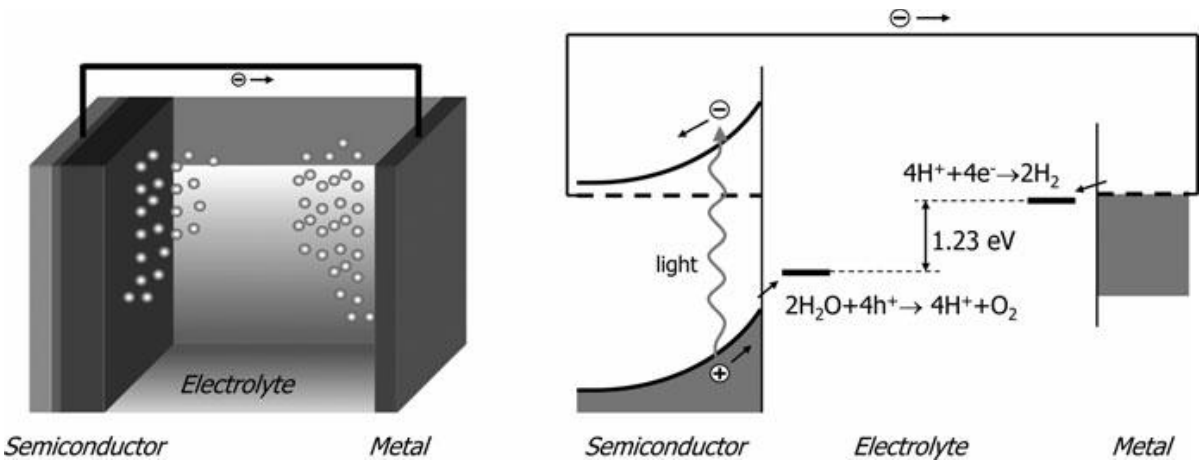

Figure 1.8 Schematic diagram of a photoelectrochemical cell with semiconductor as the anode and metal as cathode in a two-electrode cell. The left schematic illustrates the half-cell chemical reaction and minimum energy requirement for water splitting [37]. The water splitting reaction consist of two half-cell reaction, hydrogen evolution reaction (HER) referred in equation 1.8 and oxygen evolution reaction (OER) refereed in equation 1.9. The HER occurs at the semiconductor or photoanode electrode while OER occurs at the metal electrode. The minimum thermodynamic voltage required for water splitting reaction to occur is 1.23eV.

Anode:

$$2H_2O_l + 4h^+ \rightarrow 4H^+{}_{aq} + O_{2_g} \quad (1.9)$$

Cathode:

$$4H^+{}_{aq} + 4e^- \rightarrow 2H_{2_g} \quad (1.9)$$

Water Splitting Complete Reaction

$$2H_2O_l + 4H^+_{aq} \rightarrow 2H_{2_g} + O_{2_g} (1.10)$$

There are two types of semiconductor, p-type and n-type semiconductor. N-type semiconductor has a different water splitting reaction than p-type semiconductor at both working and counter electrode. N-type semiconductor possesses a suitable conduction band energy level, the water is oxidized to O_2 on the semiconductor electrode, H^+ ions dissolved into the electrolyte and e^- get transferred to the counter electrode. In counter electrode, the H^+ ions in electrolyte experience reduction to form H_2. On the other hand, p-type semiconductor, water is reduced on the semiconductor surface to form H_2 and water is oxidized on the counter electrode to from oxygen. Both p-type and n-type semiconductor PEC water splitting reactions are illustrated in figure 1.9.

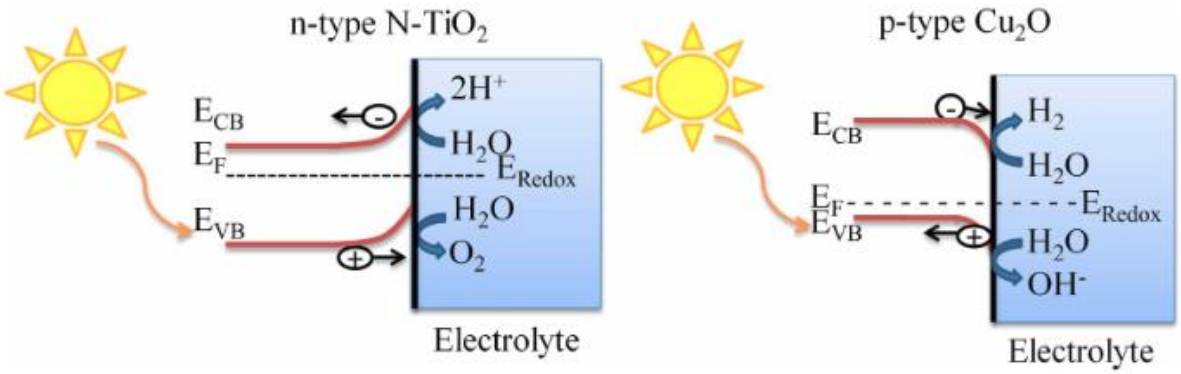

Figure 1.9 Schematic illustrated the photoelectrochemical water splitting reaction of n-type semiconductor and p-type conductor [38]

The key requirements for the selection of semiconductor for PEC water splitting are the absorption of visible light and good charge transportation [37]. Oxide semiconductor such as Cu_2O has been extensively researched due to the fulfilment of small bandgap criteria. However, oxide semiconductors are conduction band edge energies are often not optimally

positioned to produce hydrogen and prone to corrosion [39]. The Shockley-Queisser limit graph as shown in figure 1.10 can be utilized to estimate the maximum efficiency of a single junction solar cell material under sunlight as a function of the semiconductor band gap energy [40]. The Shockley-Queisser limit is the calculation for amount of electrical energy that is extracted from the semiconductor per incident photon. The maximum efficiency occurs at band gap of 1.34eV [41]. Based on the Shockley-Queisser limit graph, Cu_2O is a *p*-type semiconductor with a direct band gap of 2.0–2.2 eV, which is suitable for photovoltaic conversion with an approximate maximum efficiency of 18%.

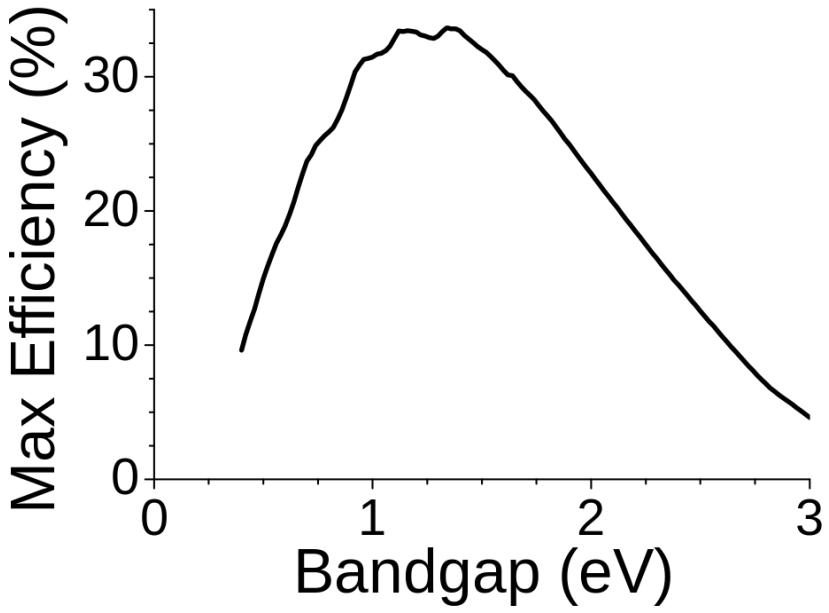

Figure 1.10 Schematic represents the maximum efficiency of a single-junction solar cell under sunlight conditions (AM 1.5 solar spectrum) as a function of band gap [40]

1.4 References

[1] Spennemann, Dirk. (2015). Techniques in Historic Preservation: Why do corroded corrugated iron roofs have a striped appearance?. 10.13140/RG.2.1.1941.9607.

[2] Libretexts. “11.6: Corrosion.” Chemistry LibreTexts, LibreTexts Libraries, 21 Mar. 2017, chem.libretexts.org/Textbook_Maps/General_Chemistry/Map%3A_Chemistry_(Zumdahl_and_Decoste)/11%3A_Electrochemistry/11.6%3A_Corrosion.

[3] “Dissimilar Metals in Contact.” *American Galvanizer's Association*, American Galvanizer's Association, 2018, galvanizeit.org/design-and-fabrication/design-considerations/dissimilar-metals-in-contact.

[4] Mouritz, Adrian P. *Introduction to aerospace materials*. Elsevier, 2012.

[5] Ramgopal, Thodla, P. I. Gouma, and G. S. Frankel. "Role of grain-boundary precipitates and solute-depleted zone on the intergranular corrosion of aluminum alloy 7150." *Corrosion*58.8 (2002): 687-697.

[6] Zhang, Weilong, and G. S. Frankel. "Transitions between pitting and intergranular corrosion in AA2024." *Electrochimica Acta* 48.9 (2003): 1193-1210.

[7] Liu, Xiaodong, et al. "Effect of applied tensile stress on intergranular corrosion of AA2024-T3." *Corrosion Science*46.2 (2004): 405-425.

[8] Jain, S. M. L. C., et al. "Spreading of intergranular corrosion on the surface of sensitized Al-4.4 Mg alloys: A general finding." *Corrosion Science* 59 (2012): 136-147.

[9] Lim, Mary Lyn C., Robert G. Kelly, and John R. Scully. "Overview of intergranular corrosion mechanisms, phenomenological observations, and modeling of AA5083." *Corrosion* 72.2 (2015): 198-220.

[10] Tedmon, C. S., D. A. Vermilyea, and J. H. Rosolowski. "Intergranular corrosion of austenitic stainless steel." *Journal of the Electrochemical Society* 118.2 (1971): 192-202.

[11] Aydoğdu, G. H., and M. K. Aydinol. "Determination of susceptibility to intergranular corrosion and electrochemical reactivation behaviour of AISI 316L type stainless steel." *Corrosion Science* 48.11 (2006): 3565-3583.

[12] Armijo, J. S. "Intergranular corrosion of nonsensitized austenitic stainless steels." *Corrosion* 24.1 (1968): 24-30.

[13] Frankel, G. S. "Pitting corrosion of metals a review of the critical factors." *Journal of the Electrochemical Society* 145.6 (1998): 2186-2198.

[14] Brunner, Gerd. "Corrosion in Hydrothermal and Supercritical Water." *Supercritical Fluid Science and Technology*. Vol. 5. Elsevier, 2014. 591-619.

[15] Kritzer, Peter. "Corrosion in high-temperature and supercritical water and aqueous solutions: a review." *The Journal of Supercritical Fluids* 29.1-2 (2004): 1-29.

[16] Burleigh, T. D. "The postulated mechanisms for stress corrosion cracking of aluminum alloys: A review of the literature 1980-1989." *Corrosion* 47.2 (1991): 89-98.

[17] Abedi, S.S., A. Abdolmaleki, and N. Adibi, *Failure analysis of SCC and SRB induced cracking of a transmission oil products pipeline.* Engineering Failure Analysis, 2007. **14**(1): p. 250-261.

[18] AlAbbas, F.M., et al., *Influence of sulfate reducing bacterial biofilm on corrosion behavior of lowalloy, high-strength steel (API-5L X80).* International Biodeterioration & Biodegradation, 2013. **78**: p. 34-42.

[19] Fassina, P., et al., *Influence of Hydrogen and Low Temperature on Pipeline Steels Mechanical Behaviour.* 11th International Conference on the Mechanical Behavior of Materials (Icm11), 2011. **10**: p. 3226-3234.

[20] Fallahmohammadi, E., F. Bolzoni, and L. Lazzari, *Measurement of lattice and apparent diffusion coefficient of hydrogen in X65 and F22 pipeline steels.* International Journal of Hydrogen Energy, 2013. **38**(5): p. 2531-2543.

[21] Arafin, M.A. and J.A. Szpunar, *A novel microstructure - Grain boundary character based integrated modeling approach of intergranular stress corrosion crack propagation in polycrystalline materials.* Computational Materials Science, 2010. **47**(4): p. 890-900.

[22] Fassina, P., et al., *Effect of hydrogen and low temperature on fatigue crack growth of pipeline steels.* Engineering Fracture Mechanics, 2013. **103**: p. 10-25.

[23] Floro, J. A., et al. "Biaxial moduli of coherent Si 1− x Ge x films on Si (001)." *Applied physics letters* 71.12 (1997): 1694-1696.

[24] Honda, N., et al. "In situ stress measurements of sputter-deposited films." *Sensors and Actuators A: Physical* 62.1-3 (1997): 663-667.

[25] Koch, R. "The intrinsic stress of polycrystalline and epitaxial thin metal films." *Journal of Physics: Condensed Matter* 6.45 (1994): 9519.

[26] Stoney, George Gerald. "The tension of metallic films deposited by electrolysis." *Proc. R. Soc. Lond. A* 82.553 (1909): 172-175.

[27] Feng, X., Y. Huang, and A. J. Rosakis. "On the Stoney formula for a thin film/substrate system with nonuniform substrate thickness." *Journal of Applied Mechanics* 74.6 (2007): 1276-1281.

[28] Wang, J., P. Shrotriya, and K-S. Kim. "Surface residual stress measurement using curvature interferometry." *Experimental Mechanics* 46.1 (2006): 39-46.

[29] Çapraz, Ömer Özgür, Kurt R. Hebert, and Pranav Shrotriya. "In situ stress measurement during aluminum anodizing using phase-shifting curvature interferometry." *Journal of The Electrochemical Society* 160.11 (2013): D501-D506.

[30] Van Overmeere, Quentin, Frédéric Blaffart, and Joris Proost. "What controls the pore spacing in porous anodic oxides?." *Electrochemistry Communications* 12.9 (2010): 1174-1176.

[31] Çapraz, Ömer Özgür, et al. "Role of oxide stress in the initial growth of self-organized porous aluminum oxide." *Electrochimica Acta* 167 (2015): 404-411.

[32] Çapraz, Ömer Özgür, Pranav Shrotriya, and Kurt R. Hebert. "Measurement of stress changes during growth and dissolution of anodic oxide films on aluminum." *Journal of The Electrochemical Society* 161.5 (2014): D256-D262.

[33] Çapraz, Ömer Özgür, et al. "Factors controlling stress generation during the initial growth of porous anodic aluminum oxide." *Electrochimica Acta* 159 (2015): 16-22.

[34] Ide, Shinsuke, et al. "Oxide Microstructural Changes Accompanying Pore Formation During Anodic Oxidation of Aluminum." *Electrochimica Acta* 232 (2017): 303-309.

[35] Ö.Ö. Çapraz, S. Ide, P. Shrotriya, K.R. Hebert, Tensile stress and plastic deformation in aluminum induced by aqueous corrosion, Acta Mater., 115 (2016) 434-441.

[36] Yavas, Denizhan, et al. "Morphology and stress evolution during the initial stages of intergranular corrosion of X70 steel." *Electrochimica Acta* 285 (2018): 336-343.

[37] Van de Krol, Roel. "Principles of photoelectrochemical cells." *Photoelectrochemical hydrogen production*. Springer, Boston, MA, 2012. 13-67.

[38] C V, Niveditha & a C, Nizamudeen & Ram, Rajita & Mj, Jabeen & Sindhu, Swaminathan. (2018). Showcasing electrode -electrolyte interfacial potential as a vital parameter in the hydrogen generation by metal oxides electrodes. Materials Research Express. 5. 10.1088/2053-1591/aab076.

[39] Hodes, G., Fonash, S.T., Heller, A., Miller, B.: In: Gerischer, H. (ed.) Advances in electrochemistry and electrochemical engineering. Wiley, New York (1985)

[40] William Shockley and Hans J. Queisser, "Detailed Balance Limit of Efficiency of p-n Junction Solar Cells", Journal of Applied Physics, Volume 32, pp. 510-519 (1961)

[41] Rühle, Sven. "Tabulated values of the Shockley–Queisser limit for single junction solar cells." *Solar Energy* 130 (2016): 139-147.

[42] Snow, Dennis A., ed. *Plant engineer's reference book*. Elsevier, 2001.

CHAPTER 2. IN-SITU STRESS DEVELOPEMENT ASSOCIATED WITH INTERGRANULAR CORROSION OF ALUMINUM AA2024 AND AA5083

2.1 Introduction

Aluminum 2XXX and 5XXX series alloys has been widely utilized in recent years in commercial aerospace and marine applications due to its high strength to weight ratio, low cost and great corrosion resistance [1, 2, 5, 6-9]. Aluminum Association (AA) 2024-T3, Al-Cu-Mg alloy and AA5083-H116, Al-Mg alloy are the target aluminum alloys in this study since both are widely used in the industries. However, both aluminum alloys are susceptible to intergranular corrosion (IGC) due to the principal alloying elements in the material. IGC is the metal degradation along the selective grain boundary elements in a corrosive environment. The surface damage or localized corrosion initiated at the grain boundaries that relates to IGC may further lead to intergranular stress corrosion cracking (IGSCC), a type of fatigue and brittle failures found in metal alloys due to the initiation of microscopic cracks on the material surface under a tensile stress [16]. IGC might be the initial surface damage that may lead to catastrophic events with sudden and unpredictable failure on the applications of the materials. The general interest is to investigate whether the corrosion localization on the material surface relates to the material failure mechanisms.

The current understanding of IGC of aluminum alloys is the presence of the intermetallic particles that precipitates along the grain boundaries which will induce localized corrosion on the material surface. AA2024 and AA5083 has different localized corrosion behavior even though both alloys have principal alloying elements that contributed to the formation of intermetallic particles that possibly induces corrosion under specific condition. S phase (Al_2CuMg) particles is one of the intermetallic particles found in AA2024 which contributed to the IGC in corrosive environment. The anodic S phase particles stimulates the

dealloying process of principal alloying elements from the matrix body leaving rich copper (Cu) particles [1, 2, 5]. The rich Cu particles formed galvanic couples with the matrix body which further stimulate the dissolution of the matrix body [2, 5]. The dissolution of S phase particles directed to the localized corrosion which propagated into the matrix body and along the grain boundaries. On the other hand, AA5083 is susceptible to IGC when exposed to long term elevated temperature in a corrosive environment [6-9]. The supersaturated Mg diffuses along the grain boundaries leading to the formation of β phase particles through sensitization process with the condition that AA5083 containing more than 3wt% Mg [7, 8]. The selective preferential dissolution of β phase particles along the grain boundaries induced IGC. Recent evidence suggested that the preferential dissolution of intermetallic particles of AA2024 along the grain boundaries resulted in the formation of aluminum oxide. The evidence had led to the hypothesis that the formation of oxide of AA2024 and AA5083 along the grain boundaries provided the driving force for the compressive stress generation which further developed into IGC. However, the formation of oxide for both aluminum alloys are different. The oxide formation for AA2024 and AA5083 are suspected to be caused by the matrix oxidization and β particles oxidization.

In this work, in-situ stress measurements have been utilized to monitor the mechanical stress evolution during anodic dissolution of the aluminum alloy which resulted in the internal oxide formation along the grain boundaries. Scanning Electron Microscope (SEM) and Energy-Dispersive Spectrometer (EDS) also been utilized to characterize the morphology of the corroded aluminum alloy. The present results acquired along with the recent studies helped verified the internal oxidation of the aluminum alloys during dissolution gave rise to large compressive stress development which may further led to IGC.

2.2 Experimental

2.2.1 Materials and Methods

2.2.1.1 Aluminum and Composition

High strength AA2XXX series alloy, AA2024-T3 specimens were machined into rectangular coupons with dimensions of 20 mm x 30 mm (W x L) from commercially acquired sheet (McMaster-Carr) with thickness of 1.27 mm. Marine-Grade Aluminum Alloy, AA5083-H116 specimens were cut and milled into rectangular coupons with dimensions of 25 mm x 35 mm x 1 mm (W x L x T) from commercially acquired sheet (McMaster-Carr). The chemical compositions of AA2024-T3 and AA5083-H116 specimens were shown in Table 2.1 according to ASTM E1251 and ASTM B928 standard. Both groups of cut specimens were cleaned attentively with acetone and ethanol (C_2H_5OH) to remove any impurities from the specimens' surface, rinsed with plenty of deionized water, then air dried for further use.

Table 2. 1 Chemical Compositions of AA2024 and AA5083-H116

Alloy	Si	Fe	Cu	Mn	Mg	Other	Al
2024-T3	0.08	0.19	4.5	0.61	1.3	0.16	Rest
5083-H116	0.4	0.4	0.1	0.40 - 1.10	4.00 - 4.90	0.65 - 0.86	Rest

2.2.1.2 Sensitization and NAMLT measurement

One group of cut AA5083-H116 specimens were sensitized at 100 degree Celsius for 200 hours continuously without any prior treatment. The IGC susceptibility of as-received and sensitized AA5083-H116 specimens were tested with ASTM G67-13, the standard test method for the Nitric Acid Mass Loss Test (NAMLT) [10]. Both faces of as-received and sensitized AA5083-H116 specimens with dimension of 1.5 cm x 2 cm x 0.1 cm (W x L x T)

were polished in ethanol with 600 grit silicon carbide (SiC) paper, rinsed with acetone and ethanol then air dried prior to NAMLT test. The degree of sensitization (DoS) for each sample was determined by calculating mass loss per unit sample area (mg/cm^2), then averaged between results from two tests.

2.2.2 Electrochemical tests and in-situ stress measurement

In-situ stress measurements using phase shifting curvature interferometry has provided advantage to measure the surface curvature change on the sample surface resulting from stress induced during electrochemical testing. This technique has proven to be effectively monitored the sample curvature and stress development during anodizing and corrosion of aluminum specimens and anodic dissolution of X70 steel [11-15]. A detailed description about the theory and procedure of using phase-shifting curvature interferometry for in-situ stress measurements was mentioned elsewhere [13]. AA2024-T3 and sensitized AA5083-H116 samples were cut and polished then mounted on the electrochemical cell with the front surface exposed to naturally aerated solution (aqueous 1 M NaCl for AA2024-T3, aqueous 0.6 M / 3.5 wt% NaCl for sensitized AA5083-H116) at room temperature while the mirror polished back surface was utilized for in-situ stress measurements. The face of the sample in-contact with solution was mounted with vacuum grease around the peripheral to prevent leakage of electrolyte solution while the opposite face of the sample was exposed to the optical system from laser interferometer. The solution facing specimen surface was polished with 600-grit polishing pads alongside ethanol, followed by cleaning with acetone and ethanol then air dried. The opposite specimen surface was polished with 600, 1000-grit polishing pads alongside with ethanol, followed by polishing cloth with 1µm diamond

suspension to maximize the flatness and mirror reflective surface of the specimen, then rinsed thoroughly with acetone and ethanol then air dried.

All electrochemical tests were performed in a three-electrode cell with platinum (Pt) wire counter electrode (CE), Ag/AgCl reference electrode (RE) and specimen surface as working electrode (WE) using a potentiostat (Gamry Instrument Potentiostat Reference 3000). Anodic potentiodynamic polarization was performed at a scan rate of 0.167 mV/s starting from -0.9 V to -0.3 V followed by a 30-minute open circuit potential (OCP). Subsequently, the samples were held at 0.1 V above the OCP value (-0.535 V for AA2024 samples and -0.63 V for sensitized and unsensitized AA5083) to monitor stress development during anodic dissolution. Current density of the specimens during anodic dissolution were calculated using the ratio of current recorded over the specimen exposed surface area (2.4 cm^2). Curvature and stress changes on the surface of the samples were monitored using phase-shifting curvature interferometry while running all the electrochemical tests. The measured curvature changes were used to calculate the stress development (force per unit width change, dF) on the surface of specimen during corrosion using Stoney Thin-Film approximation.

2.2.3 SEM and EDS Characterization

FEI Quanta 250 FEG Scanning Electron Microscope (SEM) and Oxford Aztec Energy-Dispersive Spectrometer (EDS) were utilized to characterize the surface microstructure of the corroded surfaces of aluminum alloys. The corroded samples were cut into designated size and mounted at a shallow angle (approximately $1\text{-}3^0$) with ProbeMet conductive compression mounting compound prior to polishing. The mounted specimens were polished by 600 and 1000 grit polishing pads in ethanol followed by 1µm diamond

suspension and a polishing cloth, next rinsed thoroughly with acetone and ethanol then air dried. The polishing process helped minimize the effect of scratches and impurities on image during the SEM surface characterization.

2.3 Results

2.3.1 Degree of Sensitization

The average DoS value for two as-received and sensitized specimens were 23.8 and 64.3 mg/cm^2 respectively. According to ASTM G67-13, if DoS ranging from 25 to 75 mg/cm^2, then the sample will be considered highly sensitized [10]. These results had proven that the two different conditions of samples as being as-received and sensitized.

2.3.2 Potentiodynamic Scan and Stress Measurement

The anodic potentiodynamic polarization curves of as-received AA2024 in 1M NaCI aqueous solution, as-received AA5083 and sensitized AA5083 in 0.6 M NaCI aqueous solution at scan rate of 0.167 mV/s are plotted in figure 2.1. The active OCP where material is susceptible to IGC for as-received AA2024 is -0.635 V vs (Ag/AgCl) reference electrode while as-received AA5083 is -0.726 V vs (Ag/AgCl) reference electrode and sensitized AA5083 is -0.731 V vs (Ag/AgCl) reference electrode. The OCP of sensitized AA5083 is about 5mV lower than the as-received AA5083.The rate of the dissolution of the material phase is comparatively lower at lower breakdown potential, upon reaching the breakdown potential, the rate of dissolution increases. [2] The samples were held at a potential of 0.1 V

above its respectively active OCP to monitor the stress development and current transient during IGC according to the anodic polarization curve.

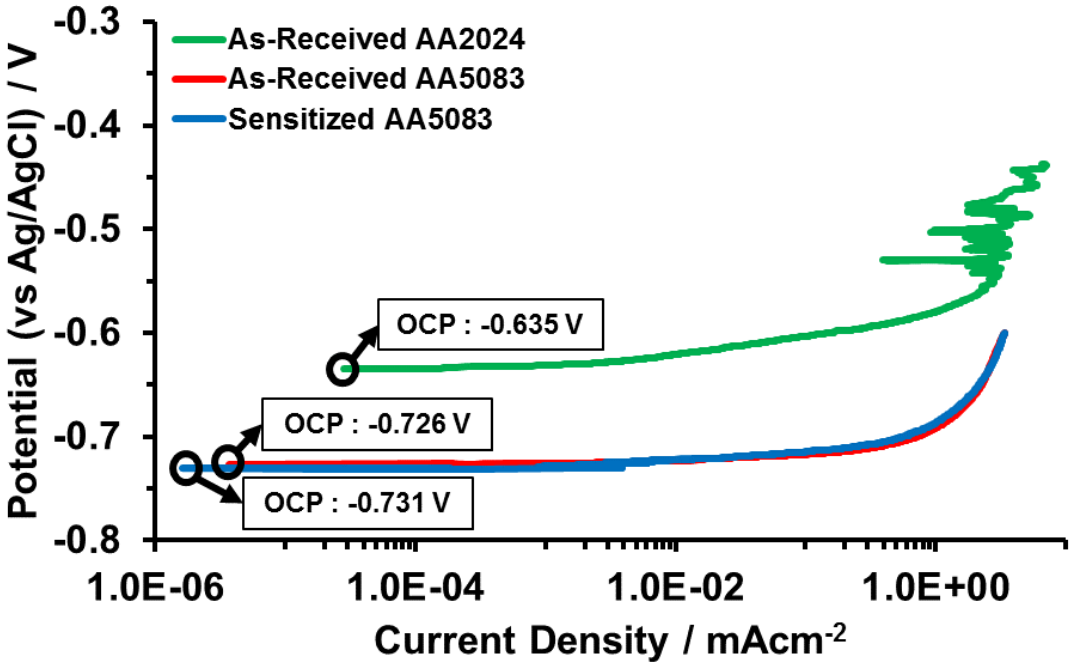

Figure 2.1 Potentiodynamic polarization curves of 2024 T3 alloy in 1 M NaCI solution while 5083 H116 alloy and sensitized 5083 H116 alloy in 0.6 M NaCI solution.

Figure 2.2 presented force per width change and current density evolution of as-received AA2024 and sensitized AA5083 across potential ranging from -0.8 V vs (Ag/AgCl) reference electrode to -0.52 V vs (Ag/AgCl) reference electrode during potentiodynamic polarization in anodic direction. Dotted lines refer to current density axis while solid lines refer to force per width axis. Force per width and current density of as-received AA2024 and sensitized AA5083 increased steadily in compressive direction after reaching OCP of -0.635 V vs (Ag/AgCl) reference electrode and -0.731 V vs (Ag/AgCl) reference electrode respectively. Both aluminum sample have negative force per width change which

corresponds to the compressive stress development due to the oxide formation on the sample surface.

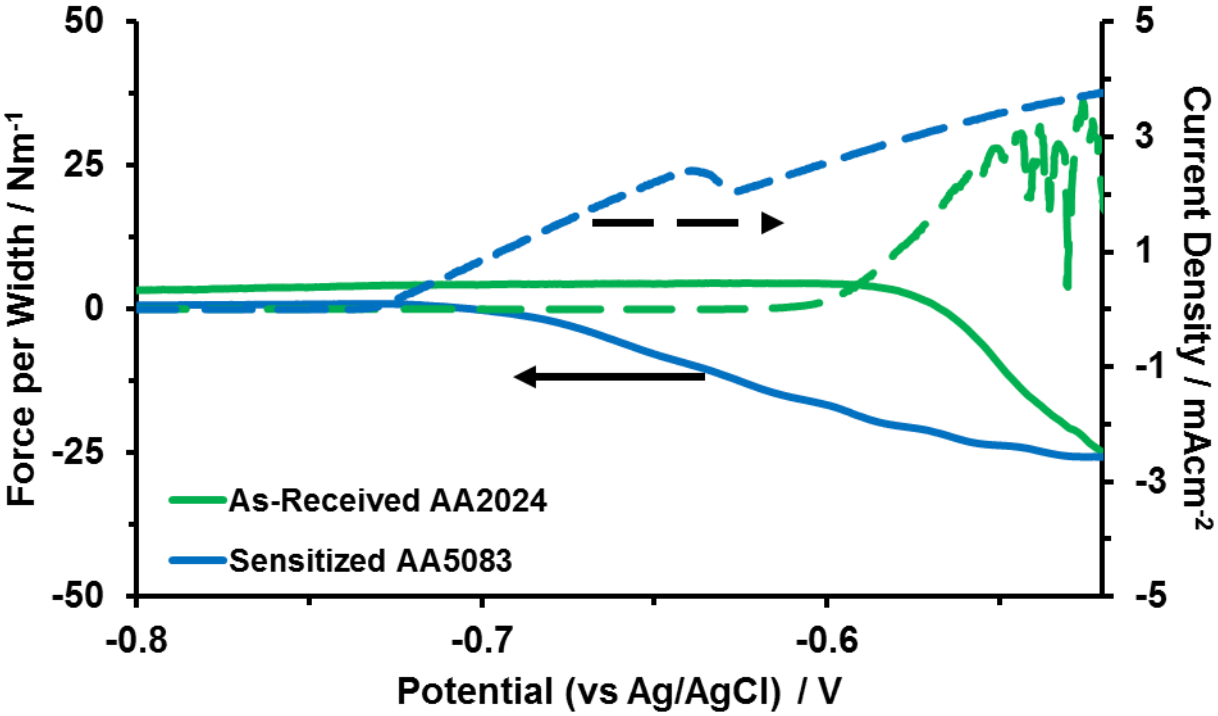

Figure 2.2 Force change and current density evolution during the Potentiodynamic polarization scan on AA2024 and AA5083 from -0.8V to -0.52V at 0.167mV/s scan rate. Negative force change corresponds to compressive stress development during the oxide formation. Dotted line corresponded to current density evolution while solid line corresponded to force per width change.

Figure 2.3 shows slope of force per width change and current density evolution of as-received AA2024 and sensitized AA5083 across potential ranging from -0.8V to -0.52V during anodic potentiodynamic polarization. Figure 2.3 gave a more precise indication of which potential gave increase to the force per width and current density. Black dots represented the smoothened version of the force per width change slope data.

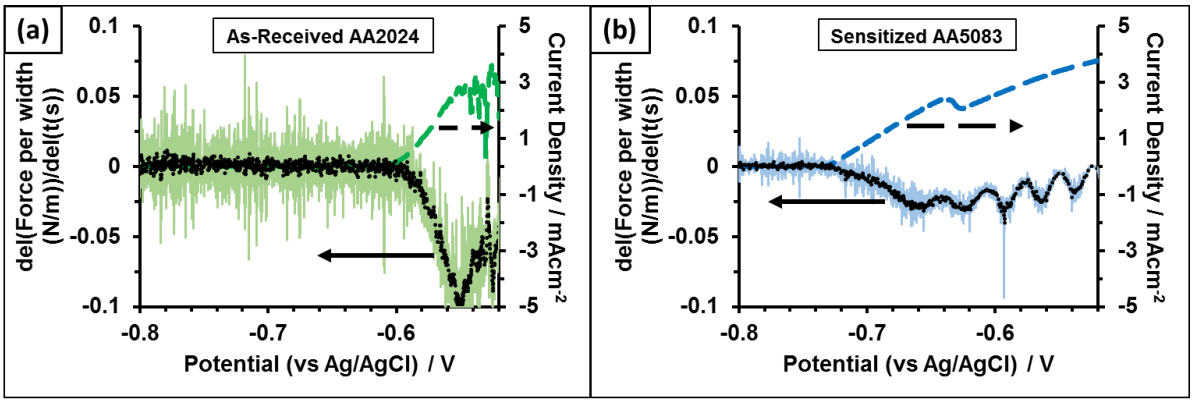

Figure 2.3 Slope of Force change and current density evolution during the Potentiodynamic polarization scan on AA2024 and AA5083 from -0.8V to -0.52V at 0.167mV/s scan rate. Black dots correspond to the slope data in smoothened version. Dotted line corresponded to current density evolution while solid line corresponded to slope of force per width change.

2.3.3 Anodic Dissolution and Stress Measurement

In-situ stress measurement associated with the intergranular corrosion of as-received AA2024, as received AA5083 and sensitized AA5083 are presented in figure 2.4 to study the relationship between the force per width change and current density evolution during IGC. Dotted lines refer to current density axis while solid lines refer to force per width axis. Figure 2.4 displayed force per width change and current density evolution of respective material for 30 minutes Open Circuit Potential (OCP) followed by one hour of anodic dissolution at 0.1 V above OCP. The results of figure 2.4 indicated there were no change in force per width and current density for all three samples during the 30 minutes OCP as the samples were located at the corrosion free zone. Force per width change for as-received AA2024 and sensitized AA5083 developed rapidly upon the start of anodic dissolution where the potential of the working electrode is stepped 0.1 V above the OCP while as-received AA5083 remained unchanged which indicates no stress generation. The maximum force per width change recorded in figure 2.4 for as-received 2024 and sensitized 5083 were -132.62 Nm^{-1} and -

156.46 Nm^{-1} respectively. Negative force per width corresponds to the compressive stress generation under the influence of oxide formation. The current density for all three samples increased sharply as soon as the anodic dissolution began, with current of density of AA2024 reaching 6$mAcm^{-2}$, while as-received AA5083 and sensitized AA5083 quickly reached the peak current density in the first 5 minutes of the anodic dissolution and slowly decreased to an average of 2.7 $mAcm^{-2}$ and 2.3 $mAcm^{-2}$ respectively. The current density evolution between the as-received AA5083 and sensitized AA5083 is 0.4 mA cm^{-2}.

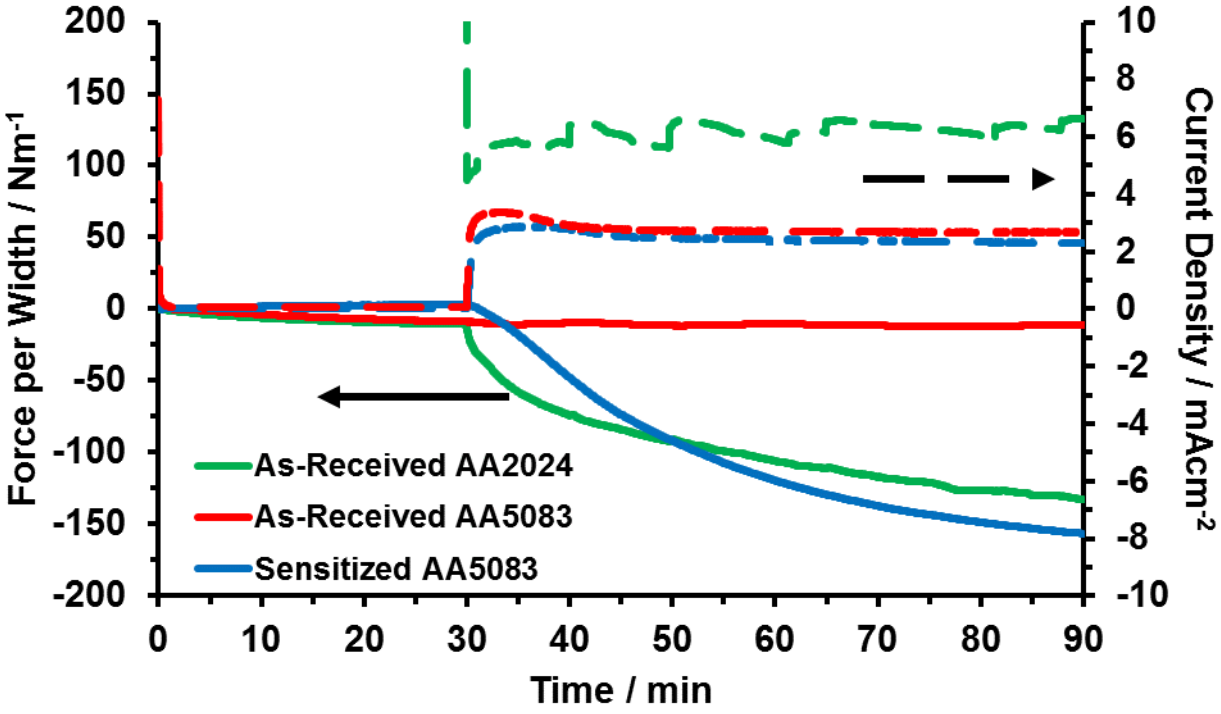

Figure 2.4 Force change and current density evolution of as-received AA2024 and as-received and sensitized AA5083 for 30 minutes OCP followed by 1 hour anodic dissolution at 0.1 V above the breakdown potential. Solid lines correspond to force per width change while dotted lines correspond to the current density evolution.

2.3.4 SEM images of the corroded surfaces

Figure 2.5 demonstrates the Scanning Electron Micrograph and Energy-dispersive X-ray Spectrographs of AA2024-T3 aluminum alloy after one hour of anodic dissolution at 0.1

V above OCP in 1 M NaCI aqueous solution with figure 2.5 (a) showing the grain boundary morphology at 5000X magnification while figure (b) and (c) showed O and Mg element map respectively. Figure 2.5 (b) indicated the grain boundary was attacked significantly where oxide was filled along the grain boundary.

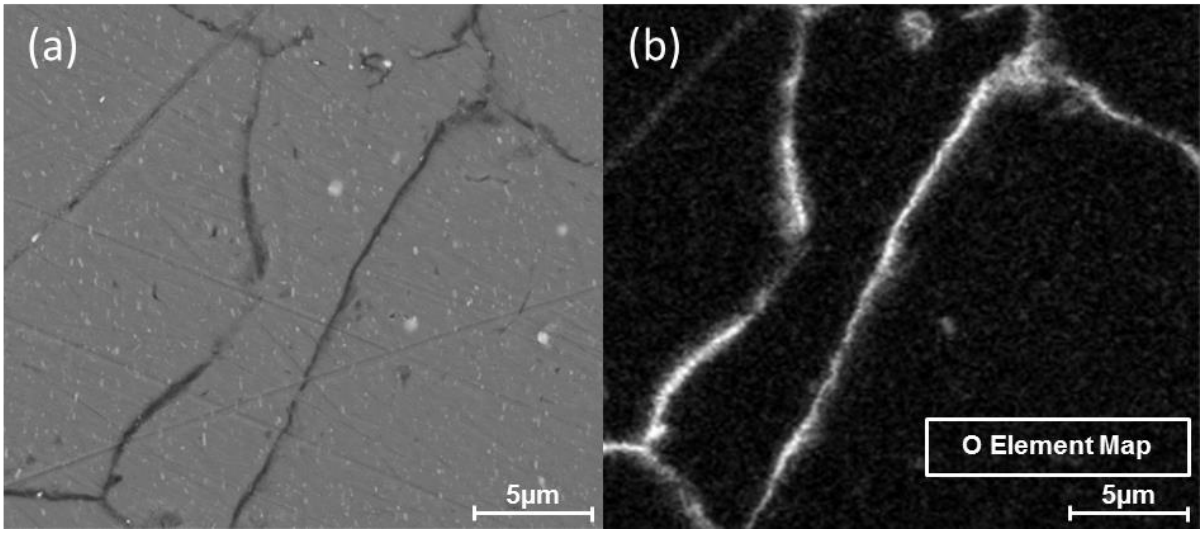

Figure 2.5 Cross section view of AA2024 after 1 hour anodic dissolution at -0.535 V where sample was prepared by shallow-angle polishing. Panel (a) is Scanning Electron Microscope (SEM) image at 5000x magnification while panels (b) is the Energy-dispersive X-ray Spectroscopy (EDS) images of each respective chemical element.

Figure 2.6 demonstrates the Scanning Electron Micrograph and Energy-dispersive X-ray Spectrographs of sensitized AA5083-H116 aluminum alloy after one hour of anodic dissolution at 0.1 V above OCP in 0.6 M NaCI aqueous solution with figure 2.6 (a) showing the grain boundary morphology at 5000X magnification while figure (b) and (c) showed O

element map. Figure 2.6 (b) indicated the grain boundary was attacked significantly where oxide was filled along the grain boundary.

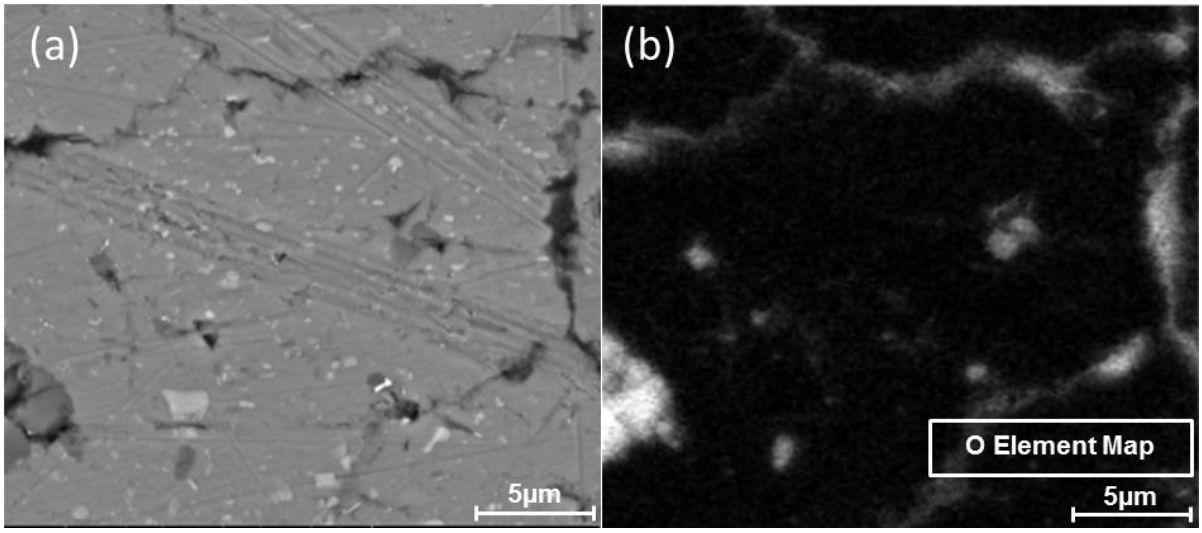

Figure 2.6 Cross section view of sensitized AA5083 after 1 hour anodic dissolution at -0.631 V where sample was prepared by shallow-angle polishing. Panel (a) is Scanning Electron Microscope (SEM) image at 5000x magnification while panels (b) is the Energy-dispersive X-ray Spectroscopy (EDS) images of each respective chemical element.

2.4 Discussion

The secondary phase or intermetallic particles in AA2024 and AA5083 played a huge role in localized corrosion. The corrosion behavior of both AA2024 and AA5083 intermetallic particles are different. Intergranular corrosion of AA2024 is enhanced by the precipitation of S-phase (Al_2CuMg) particles unlike other secondary phase particles. The S-phase particles do not dissolve during the anodic dissolution instead it undergoes a dealloying process. [1-5] S-phase particles tend to be more anodic than the matrix body which lead to the selective dissolution of magnesium (Mg) and aluminum (Al) components. The dealloying of magnesium (Mg) and aluminum (Al) components from the S-phase particles will leave copper (Cu) rich remnants in the grain boundaries. The remnants of S-

phase particles act as a cathode that lead to the preferential dissolution of matrix body due to the formation of galvanic couple which further drive localized corrosion along the grain boundaries forming deep trenches as mentioned by Hashimoto and et.al [5]. X. Zhou indicated the continuous localized corrosion at the dealloyed S-phase particle not only propagated deeper into the matrix body adjacent to the particle but also formation of IGC due to the attacked of grain boundaries. [4] The dissolution of Al from the matrix body along the grain boundaries results in the formation of oxide due to Al matrix oxidation.

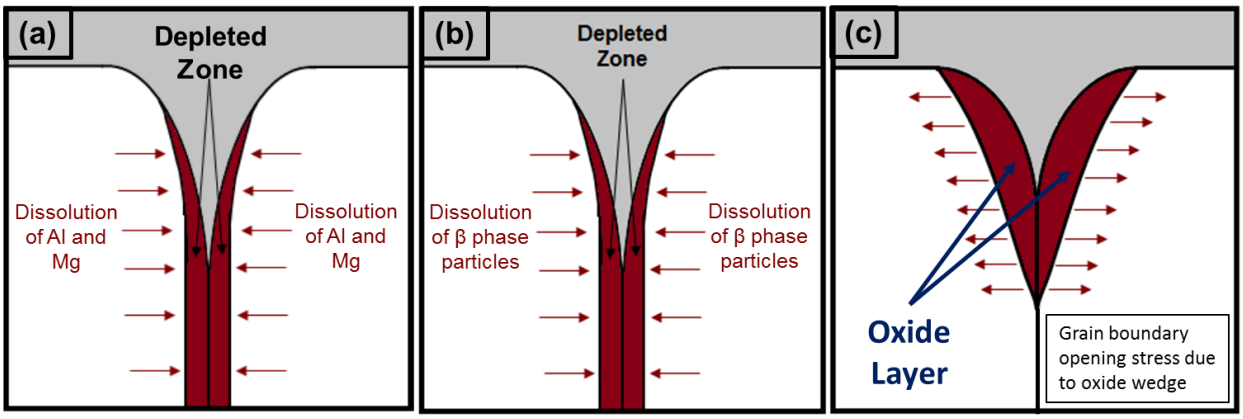

Figure 2.7 (a) Schematic of the dissolution of Al and Mg from the S-phase particles in AA2024 (b) Schematic of the dissolution of β phase particles in AA5083 (c)

Schematic 2.7 (c) depiction of oxide wedge morphology of intergranular corrosion. The sensitization process resulted in the precipitation of β phase particles along the grain boundaries of AA5083 which will lead to the IGC of AA5083. The galvanic coupling between the β phase particles and Al matrix body provide the driving force to the preferential dissolution of β phase particles along the grain boundaries during anodic dissolution process in electrolyte. [6-8] The dissolution of β phase particles lead to the formation of oxide along the grain boundary. The formation of oxides along the grain boundaries induced the expansion of the volume along the grain boundaries. The increase in the volume in grain

boundaries acted as a wedge which induced wedging force along the grain boundaries which further opens the grain boundary resulting in compressive stress development on the respective aluminum sample body with the measurement from phase shifting curvature interferometer as shown in figure 2.8. The driving force provided by volume expansion will lead to spreading of localized corrosion further along the grain boundaries and into the matrix body.

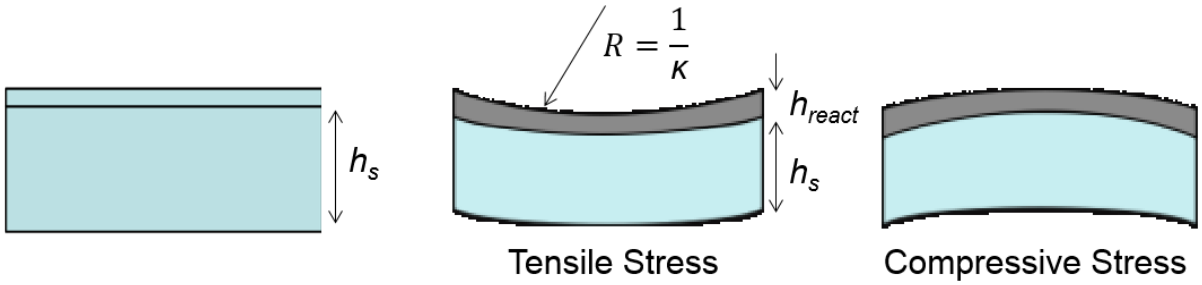

Figure 2.8 Schematic depiction of material in original, tensile and compressive state with h_s representing thickness of material body and h_{react} representing thickness of oxide.

The oxide wedge depth of the penetration as shown in figure 2.9 can be estimated using equation 2.1 with F is force per width change of the sample surface, σ_Y is the tensile yield strength of the material and d is the oxide wedge depth of the penetration. Equation 2.1 assumes the material is fully yielded. The maximum observed maximum force per width change for AA2024, AA5083 and sensitized AA5083 are 132.73 N/m, 11.44 N/m and 156.47 N/m respectively as shown in figure 2.4. The tensile yield strength of AA2024 is 345 MPa and AA5083 is 228MPa according to ASM Aerospace Specification Metals Inc. The maximum estimated oxide wedge penetration depth for AA2024, AA5083 and sensitized AA5083 using equation 2.1 are 380 nm, 50 nm and 680 nm respectively.

$$F = \sigma_Y d \quad [2.1]$$

Table 2. 2 Maximum force per Width Change, Tensile Yield Strength and Oxide Wedge Depth of Penetration for As-received AA2024, As-Received AA5083 and Sensitized AA5083.

Material	F_{max} (Nm^{-1})	σ_Y (MPa)	D (nm)
As-Received AA2024	132.73	345	380
As-Received AA5083	11.44	228	50
Sensitized AA5083	156.47	228	680

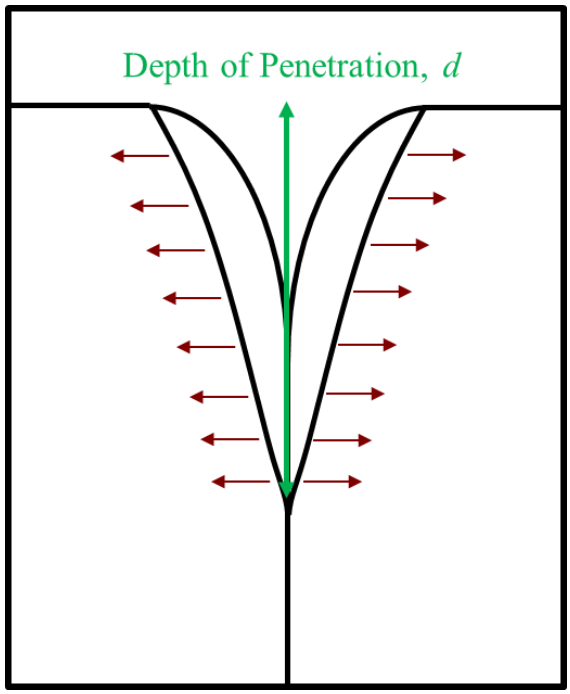

Figure 2.9 Schematic illustration of the penetration of oxide wedge depth with d representing the depth of penetration

The oxide wedge penetrates deeper into the grain boundaries which lead further develop a crack and ultimately leads to stress corrosion cracking (SCC).

2.5 Conclusion

Phase shifting curvature interferometry was integrated in an electrochemical cell to enable measurement of stress measurement during corrosion experiments. The development

of IGC is associated with the stress development on the sample surface along the grain boundaries when the secondary phase particles are attacked. The current density and force change did not occur during the OCP while current density and force started to evolve when the anodic dissolution process began. The measurement of the curvature and stress revealed compressive force developed when the sample was driven by an anodic potential. The internal oxide formation along the grain boundary of AA2024 and AA5083 resulted in the compressive stress development. The stress development results obtained in this study indicate the oxide formation induced wedging stresses in the grain boundary that may further drive the opening of crack along the grain boundary.

2.6 References

[1] Birbilis, N., and R. G. Buchheit. "Electrochemical characteristics of intermetallic phases in aluminum alloys an experimental survey and discussion." *Journal of The Electrochemical Society* 152.4 (2005): B140-B151.

[2] Guillaumin, Valérie, and Georges Mankowski. "Localized corrosion of 2024 T351 aluminium alloy in chloride media." *Corrosion Science* 41.3 (1998): 421-438.

[3] Zhang, Weilong, and G. S. Frankel. "Transitions between pitting and intergranular corrosion in AA2024." *Electrochimica Acta* 48.9 (2003): 1193-1210.

[4] Zhou, X., et al. "Study of localized corrosion in AA2024 aluminium alloy using electron tomography." *Corrosion Science* 58 (2012): 299-306.

[5] Hashimoto, T., et al. "Investigation of dealloying of S phase (Al2CuMg) in AA 2024-T3 aluminium alloy using high resolution 2D and 3D electron imaging." *Corrosion Science*103 (2016): 157-164.

[6] Searles, J. L., P. I. Gouma, and R. G. Buchheit. "Stress corrosion cracking of sensitized AA5083 (Al-4.5 Mg-1.0 Mn)." *Metallurgical and Materials Transactions A* 32.11 (2001): 2859-2867.

[7] Goswami, R., et al. "Microstructural evolution and stress corrosion cracking behavior of Al-5083." *Metallurgical and Materials Transactions A* 42.2 (2011): 348-355.

[8] Seong, Jinwook, et al. "Influence of the altered surface layer on the corrosion of AA5083." *Journal of The Electrochemical Society* 162.6 (2015): C209-C218.

[9] Seifi, M., et al. "Sensitization and remediation effects on environmentally assisted cracking of Al-Mg naval alloys." *Corrosion Science* (2018).

[10] American Society for Testing and Materials. *Standard Test Method for Determining the Susceptibility to Intergranular Corrosion of 5XXX Series Aluminum Alloys by Mass Loss After Exposure to Nitric Acid (NAMLT Test)*. ASTM International, 2004.

[11] Yavas, Denizhan, et al. "Morphology and stress evolution during the initial stages of intergranular corrosion of X70 steel." *Electrochimica Acta* 285 (2018): 336-343.

[12] Ö.Ö. Çapraz, S. Ide, P. Shrotriya, K.R. Hebert, Tensile stress and plastic deformation in aluminum induced by aqueous corrosion, Acta Mater., 115 (2016) 434-441.

[13] Ö.Ö. Çapraz, K.R. Hebert, P. Shrotriya, In Situ Stress Measurement During Aluminum Anodizing Using Phase-Shifting Curvature Interferometry, J. Electrochem. Soc., 160 (2013) D501-D506.

[14] Çapraz, Ömer Özgür, Kurt R. Hebert, and Pranav Shrotriya. "In situ stress measurement during aluminum anodizing using phase-shifting curvature interferometry." *Journal of The Electrochemical Society* 160.11 (2013): D501-D506.

[15] J. Wang, P. Shrotriya, K.S. Kim, Surface residual stress measurement using curvature interferometry, Exp. Mech., 46 (2006) 39-46.

[16] Liu, Xiaodong, and G. S. Frankel. "Effects of compressive stress on localized corrosion in AA2024-T3." *Corrosion science* 48.10 (2006): 3309-3329.

CHAPTER 3. IN-SITU STRESS DEVELOPEMENT ASSOCIATED WITH ELECTRODEPOSITION OF Cu_2O ON ITO-Au SAMPLE

3.1 Introduction

The technology and scientific advancements for the past few decades have drove the economy to rely heavily on the use of non-renewable energy source primarily on fossil fuels. The fossil fuels reserves are sufficient for centuries of usage even with the tremendous growth rate of world human population and economic development in various industries, but the key concern of fossil fuel usage is the threats that it brought towards the environment and society [1, 15-17]. Solar based photoelectrochemical (PEC) water splitting technology is a promising renewable source of energy that would shape the trend of energy usage in the future. PEC water splitting produces hydrogen gas (H_2) as an alternative fuel source that has the potential to provide clean energy source and cost-effective solutions to the society [1-19]. PEC water splitting is a process that converts solar energy to electrochemical energy. Cuprous oxide or copper (I) oxide (Cu_2O), p-type semiconductor with a direct bandgap of 2.17 eV are favourable to use in PEC hydrogen production [15 - 18]. The conduction band of Cu_2O is 0.7 V negative to the hydrogen evolution potential while the valence band lies positive to the oxygen evolution. Cu_2O has a theoretical photocurrent of -14.7 $mAcm^{-2}$ and a theoretical light-to-hydrogen conversion efficiency of 18% [17]. Cu_2O has been widely researched for various applications such as photocatalyst for solar driven water splitting of and H_2 generation, electrode for lithium ion batteries and p-type semiconductor in heterojunction with n-type ZnO for photovoltaic applications [17]. The material is low cost, abundantly available and easily produced via electrodeposition and sputtering where the production methods are simple, economical and scalable [15]. Despite all the advantages, according to Paracchino, the main limiting factor for the usage of Cu_2O as photocathode in

PEC water splitting process is the material has poor stability in aqueous solution. The material has high electron-hole recombination rate that affected the stability of the material when undergoing hydrogen evolution reaction (HER) in aqueous solution [18].

The use of gold (Au) underlayer nanostructure has been proven to improve the efficiency of solar applications [15-16, 24-30]. The Au nanostructure enhanced the light adsorption in solar applications is mainly due to the scattering events and localized surface Plasmon resonance contributions. The Au underlayer was electrodeposited at -1.2 V for 30 minutes to serve as a reflective surface for the phase shifting curvature interferometer. Phase shifting curvature interferometer system was utilized for in-situ stress measurement on samples to monitor the surface curvature change and stress development. The technique has been proven to be effectively monitored the sample curvature and stress development during corrosion and anodic oxidization of aluminum specimens [20 – 23]. In the present work, in-situ stress measurements were conducted on Au-ITO sample during Cu_2O electrodeposition to monitor the surface deflection and stress generation on the surface.

3.2 Experiment Setup

3.2.1 Experiment Materials

The chemicals used for Gold (Au) electrodeposition were gold (III) chloride trihydrate ($HAuCl_4 \cdot 3H_2O$, ≥ 99.9%) commercially acquired from Sigma Aldrich (Milwaukee, WI, USA), sodium hydroxide (NaOH, ≥ 99.1%) and hydrochloric acid (HCl, ≥ 37.0%) from Fisher Scientific (Hanover Park, IL, USA) and L-cysteine ($C_3H_7NO_2S$, ≥ 98%) from EMD Millipore (Billerica, MA, USA). Cupric sulfate pentahydrate ($CuSO_4 \cdot 5H_2O$, ≥ 98%), lactic acid ($C_3H_6O_3$, ≥ 88.5%) and potassium hydroxide (KOH, ≥ 85.8%) were chemicals used in Cu_2O electrodeposition and commercially acquired from Fisher Scientific

(Hanover Park, IL, USA). The chemicals used for photoelectrochemical measurements were sodium sulphate (Na_2SO_4) purchased from Fisher Scientific (Hanover Park, IL, USA). Indium tin oxide (ITO) coated on glass with a dimension of 25 x 25 x 1.1 mm (conductivity: 7 Ω/sq) was commercially acquired from University Wafer, Inc. (Boston, MA, USA) was used as an electrodeposition substrate and working electrode for the electrochemical experiments. Glass-ITO substrate was pre-treated with acetone, diluted hydrochloric acid (HCI) and nitric acid (HNO_3) prior to Au electrodeposition with details mentioned.
All electrochemical experiments were carried out in a three-electrode configuration setup using a potentiostat (CHI601E potentiostat, CH Instrument) that consisted of glass-ITO substrate specimen as working electrode (WE), silver-silver chloride (Ag/AgCI) electrode with saturated potassium chloride (KCI) as reference electrode (RE) and platinum (Pt) wire as counter electrode (CE). All electrodeposition and photoelectrochemical aqueous solutions were prepared using deionized water. All electrochemical experiments were conducted in ambient temperature.

3.2.2 Gold, Au layer electrodeposition

Au thin layer was coated on the glass-ITO specimen using Au precursor dissolved aqueous solution at pH3 using electrodeposition technique. The pH of the solution was adjusted by balancing between the amount of NaOH and HCI added. Au layer was electrodeposited using a three-electrode configuration setup in an electrochemical cell and detail steps were mentioned [15 - 16]. The aim of the Au thin layer was to provide a mirror-like reflective surface for the in-situ stress measurements using phase shifting curvature interferometer while utilizing the gold underlayer for Cu_2O electrodeposition and photoelectrochemical measurement. The Au layer was electrodeposited in a beaker with

$HAuCl_4 \cdot 3H_2O$ aqueous solution at a constant potential of -1.2 V for 30 minutes. The area of the sample immersed into the aqueous solution is approximately $2cm^2$.

3.2.3 Cuprous oxide, Cu_2O electrodeposition

Cuprous oxide, Cu_2O was electrodeposited on Au coated glass-ITO specimen using Cu_2SO_4 aqueous solution at pH13. The pH value of the solution was controlled by adding controlled amount of potassium hydroxide (KOH) while the solution was heated till 50 degree Celsius using a heating plate. The pH value and temperature of solution were referred to articles [15 - 16]. Au deposited glass-ITO specimens were mounted in a special designed electrochemical cell as shown in figure 3.1 for in-situ stress measurements during Cu_2O deposition and photoelectrochemical (PEC) water splitting experiments using phase shifting curvature interferometer, a technique proven to be effectively monitored the sample curvature and stress development during corrosion and anodic oxidization of aluminum specimens [3 – 6]. The Cu_2O was electrodeposited at a constant current density of - 1 $mAcm^{-2}$ for 30 minutes while recording the stress change on the surface of specimen.

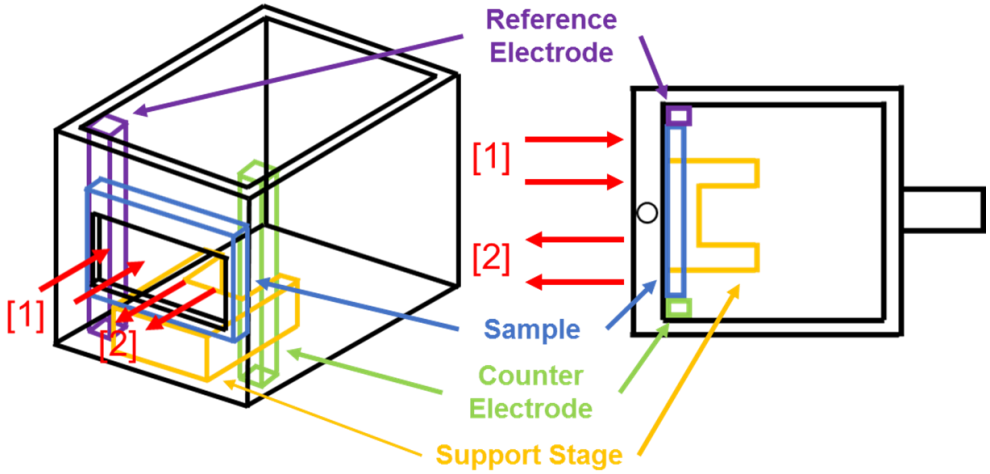

Figure 3.1 Electrochemical cell utilized for in-situ stress measurement with incoming and reflected laser beam indicated as [1] and [2] respectively, non-conductive sample surface mounted against the wall with vacuum grease while ITO coated conductive surface facing solution and support stage for holding sample in position.

3.2.5 In-Situ Curvature Phase Shifting Interferometer

3.2.5.1 Theory of surface deflection and stress development using phase shifting curvature interferometry

Phase shifting curvature interferometer utilized the interference measurement to detect deflection of sample surface when undergoing electrochemical experiments. The setup of the phase shifting curvature interferometer used is shown in figure 3.2. The notation of the optical elements in figure 3.2 are represented as mirror (M), mounted calcite beam displacer (C), beam splitter (BS), lens (L), beam block (B), quarter wave plate (Q), polarizer (P) and photodetector (PD). The main laser source used in the phase shifting curvature interferometer is Helium Neon (He-Ne) laser. The non-conductive sample surface was mounted against the wall of the electrochemical cell with vacuum grease while sitting on top of the support stage which was exposed to the two incoming laser beams and the conductive ITO surface was exposed to the aqueous solution for various electrochemical experiments. The sample surface

deflection changes are affected by the path length difference between the four laser points as shown in figure 3.3. According to figure 3.3, *c* is the distance between point A and B, *d* is the distance between midpoints of points AB and CD and *f* is the focal length of convex lens. Finite difference approximation is used to determine the relationship between the path length difference and curvature.

$$\kappa \approx \frac{d^2y}{dx^2} \approx \frac{1}{d}\left(\frac{y_A - y_B}{c} + \frac{y_D - y_C}{c}\right) = \frac{\delta}{2cd} \text{ [3.1]}$$

κ is curvature, δ is the path length change while y_A,y_B, y_C and y_D are the deflection points at points A, B, C and D. The assumptions for equation 3.1 are deflections at points A, B, C and D are small and the substrate is initially flat. Since curvature change of substrate is measured by the interference of beams, change of path length difference is time dependent where 90° phase shift is introduced. I_m is the mean intensity of beam, A is the amplitude of the measured beam intensity and $\emptyset_0$ is the initial phase of the fringe. The continuous changing of phase shift, $\emptyset(t)$ is time dependent where the intensity of interfered beam, $I(t)$ oscillates over time. To implement the phase shift in the interferometer system, the beams reflected from the surface of specimen are split into two components, one with and one without the phase shift of 90°. The intensity produced by interference of unaltered and phase shifting components are shown in equation 3.2 and 3.4.

$$I_1(t) = I_{1m} + A_1 sin(\emptyset(t) + \emptyset_0) \text{ [3.2]}$$

$$dI_1(t) = -A_1 \cos(\emptyset(t) + \emptyset_0) d\emptyset \text{ [3.3]}$$

$$I_2(t) = I_{2m} + A_2 cos(\emptyset(t) + \emptyset_0) \text{ [3.4]}$$

$$dI_2(t) = A_2 \sin(\emptyset(t) + \emptyset_0) d\emptyset \text{ [3.5]}$$

$\emptyset_0$ is the initial phase of the fringes, I_m is the mean intensity of beam and A is the amplitude of the measured beam intensity signal. Equation 3.3 and 3.5 are the differentiation of beam intensity $I_1$and I_2 to get intensity change.

$$d\emptyset = I_2(t)dI_1(t) - I_1(t)dI_2(t) \text{ [3.6]}$$

The phase change that arises from cross multiplication in equation 3.6 of beam intensity $I_1$and $I_2$and intensity change of $dI_1$and $dI_2$are substituted back into equation 3.2 to form equation 3.7.

$$d\delta = \frac{\lambda}{2\pi A_1 A_2} d\emptyset \text{ [3.7]}$$

λ is wavelength of the wave source which is 632nm for He-Ne laser. The rate of curvature change can be expressed from equation 2 to form equation 3.8.

$$d\kappa = \frac{d\delta}{2cd} \text{ [3.8]}$$

General Stoney's Thin Film Stress Equation is shown as below in equation 3.9 [21, 31-33].

$$\sigma_{xx} = \frac{E_s {h_s}^2 \kappa}{6h_f(1-v_s)} \text{ [3.9]}$$

σ_{xx} is the biaxial in-plane stress, h_s is the substrate thickness, E_s is the Young's Modulus of Elasticity of specimen, v_s is the Poisson's ratio of the specimen and $h_f$is the corroded film thickness. The assumptions for using Stoney's Thin Film Stress Equation to measure curvature change on the substrate surface according to Feng and et al are [33]:

1. Substrate thickness is very small compared to lateral dimensions
2. Ratio of corrosive film to substrate thickness is small
3. Substrate material is isotropic, homogeneous and linearly elastic
4. Strain and rotations is infinitesimal

The film thickness of the experiments conducted are difficult to measure without advance profilometer and equation 3.10 is further derived to accommodate the absence of film thickness.

$$dF = \frac{E_s {h_s}^2}{6(1-\nu_s)} d\kappa \text{ [3.10]}$$

F is the in-plane force per unit width at the substrate surface produced by dissolution process and it is no longer biaxial in-plane stress. The force per width is the biaxial in-plane stress change, σ_{xx} integrated over the thickness of the substrate in z direction as shown in figure 3.4 and can be represented as equation 11. X-axis is parallel to the substrate surface while z-axis is the direction that extends towards the thickness of the substrate.

$$F = \int_0^\infty \sigma_{xx} dz \text{ [3.11]}$$

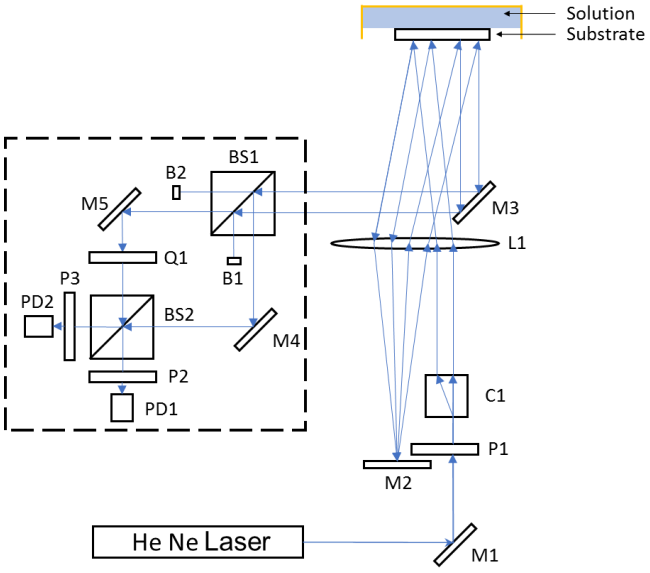

Figure 3.2 Phase shifting curvature interferometer setup arrangement of optical components and sample. Notation of the optical elements is mirror (M), mounted calcite beam displacer (C), beam splitter (BS), lens (L), beam block (B), quarter wave plate (Q), polarizer (P) and photodetector (PD). The components of the Mach-Zehnder interferometer are enclosed by the thick dashed line. Arrow of the line represents the flow of the laser through various optical components.

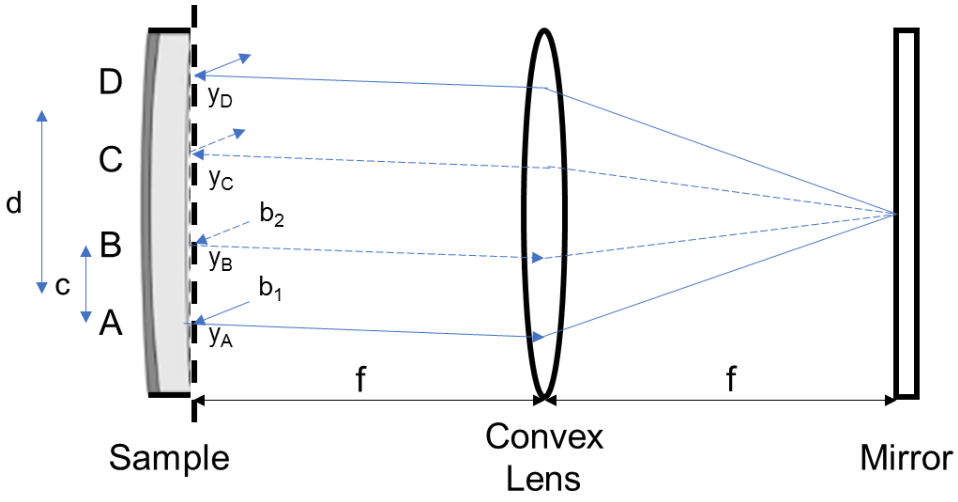

Figure 3.3 Principle of curvature interferometry with points A and B representing the incoming (b_1 & b_2) while points C and D representing the reflected laser beams on the rear surface of the sample; y_A, y_B, y_C and y_D are the horizontal distances at these points between the sample and the reference plane (indicated by the vertical dashed line). *c* is the distance between points A and B, and *d* is the distance between the midpoints of points *AB* and *CD*. *f* is the focal distance. Dark gray shading indicates the conductive sample surface layer in contact with the electrolyte [21].

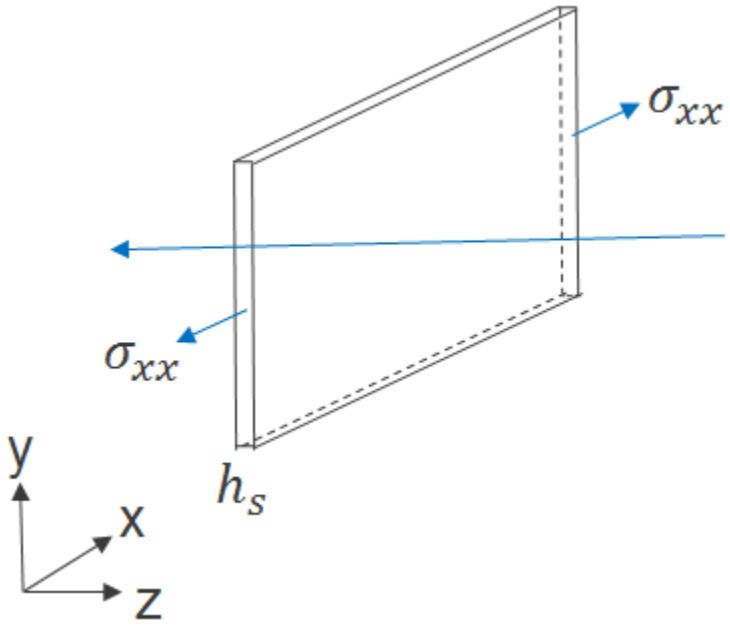

Figure 3.4 Biaxial in-plane stress across the thickness of the substrate in z-direction

3.2.5.2 The optical components and beam path directions of the phase shifting curvature interferometer

The optical components and beam path directions of the phase shifting curvature laser interferometer were illustrated in figure 2. The He-Ne laser with wavelength of 632 nm is the main laser source for the interferometer system where the incident beam is reflected 90 degrees by mirror M1. The laser beam then passed through polarizer P1 which polarized the beam at 45 degrees. The polarized beam passes through calcite C1 which splits the laser beam into two separate light beam components, vertical and horizontal respectively. The two laser beams travelled parallelly through convex lens L1 then focuses on points A and B on the sample surface opposite from the surface facing the electrolyte. The reflected beams from points A and B got focused on mirror M2 and reflected to points C and D on the sample surface. M3 reflects the laser points C and D to the phase-shifting Mach-Zehnder interferometer. The beams from points C and D were directed to a polarized beam splitter BS1 and further split into two beams. I_2 pass through quarter waveplate Q1 which converts the polarized beam from linear to circular. I_1 and I_2 meet in BS2 which is used to interfere both beams and send out identical beams. The identical beams each travelled through P2 and P3 respectively to be aligned in fast (+45 degrees) and slow (-45 degrees) axis components. The laser beams were received by respective photodetectors PD1 and PD2 which then received the laser beams signal as a form of power. The advantage of this phase shifting curvature interferometry compared to the previous developed interferometry system by Çapraz are as follow:

1. Reduced the beam intensities lost when passing through optical components as less optical components in the system

2. Allowed the incoming and reflected beams from sample surface to be identified easier with less optical components
3. Lowered the chance of beams reflected into the laser source which will greatly affect the stability and resolution of the system
4. Provided future opportunity to reduce the size of the interferometry system with smaller optical component intact in an enclosed box to ease the transportation of the interferometry system

Both phase shifting curvature interferometry system have similar Mach-Zehnder interferometer setup for mixing of beam interference and laser source.

3.3 Results and discussion

3.3.1 Resolution and stability

The resolution and stability of the phase shifting curvature interferometer system can be demonstrated with the mechanical perturbation response measurements over a period time. The stability of the phase shifting curvature interferometer system was presented in figure 3.5 with a non-reacting sample which in this case is a mirror. The reason was using mirror can accurately determine the stability of the system as mirror has excellent reflective and flat surface. Figure 3.5 displayed both interfered beam intensities acquired from power signal output from two photodetectors were normalized according to respective amplitude of the beam intensities to aid the presentation of the data. The effect of perturbation from aligning interference of the beams lasted about 5 hours before slowly died out and stabilize. The interferometer system has both intensity outputs that remained stable for nearly seven hours. The routine of stabilizing the interferometer system has been carried out every time

before conducting any electrochemical experiments to ensure the in-situ stress measurement is not affected by the noise from the interferometer system.

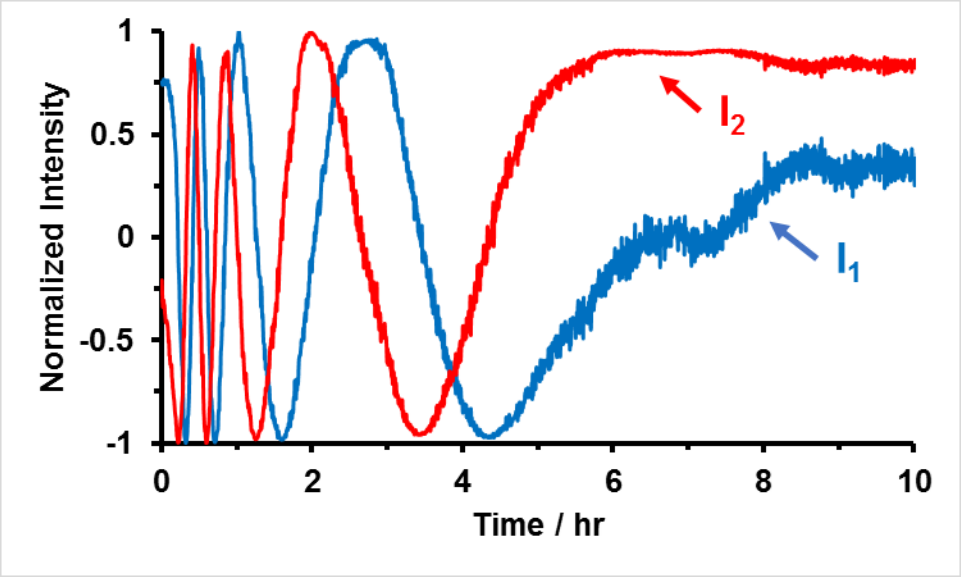

Figure 3.5 The stability of the phase shifting curvature interferometer system. The beam intensities of I_1 and I_2 were monitored and recorded starting from time zero after aligned to get beam interference. The amplitude of the intensities was used to normalize the recorded intensities.

To further understand the stability of the system, the stable section of the intensities curves was analysed to determine the smallest curvature change of the sample that the system can detect. The noise level of the system can be observed from figure 3.6 where the data points in blue represented the incremental curvature change over the interval of 20 seconds between the two curvature measurements. The noise threshold of the system for curvature measurement can be determined through the magnitude of the incremental curvature change of the system during the stable period which is roughly within 1×10^{-4} m^{-1}. The drift of the system over period of nine hours is determined through curvature change measurement as shown in figure 3.6 represented in green. The drift in the curvature change is less than 8×10^{-4} m^{-1} and drift rate of the curvature measurement is 2.5×10^{-8} $m^{-1}s^{-1}$. The noise threshold

recorded by Çapraz's phase shifting curvature interferometer system is 1 x 10^{-6} m^{-1} which is 100 times smaller in magnitude, curvature change drift is less than 1 x 10^{-4} m^{-1} and drift rate of the curvature measurement is 5 x 10^{-9} $m^{-1}s^{-1}$. The noise threshold of the interferometer system can be affected by various factor such as vibration from internal or external substance, light interference and activity from surrounding.

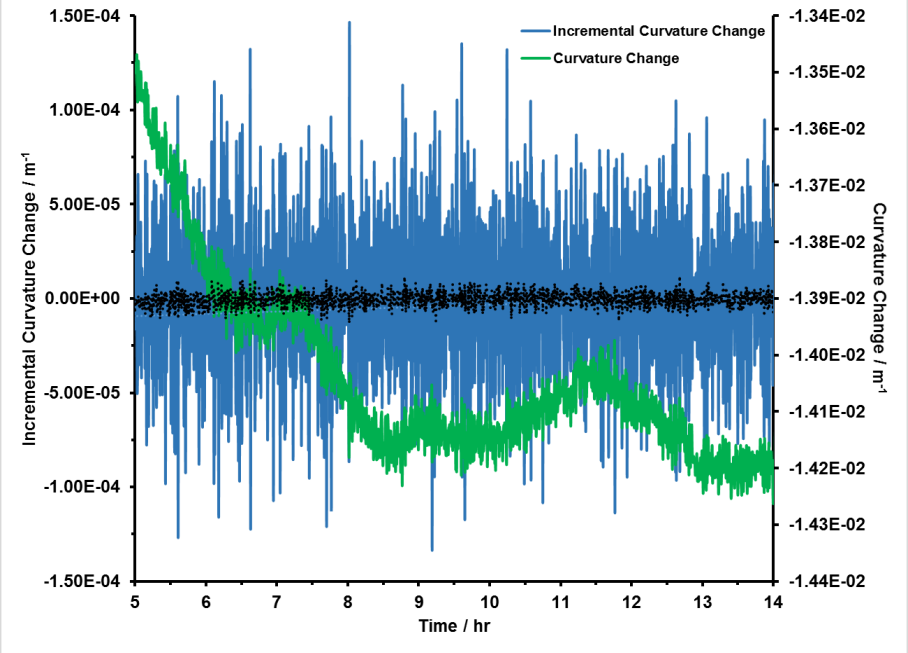

Figure 3.6 The data points in blue represented the incremental curvature change over the interval of 20 seconds between the two curvature measurements (left axis). The black dots were referred as the smothered data points of the incremental curvature change. The green line represented the curvature change over period time (right axis).

3.3.2 Stress measurement and Cu_2O electrodeposition

The force per width change and potential evolution during electrodeposition of Cu_2O on ITO coated glass surface at a constant current density of - 1 Acm^{-2} for 30 minutes with Cu_2SO_4 aqueous solution at pH13 is shown in figure 3.7 (a). Figure 3.7 (a) were zoomed into the first 5 minutes of the electrodeposition experiment to take a closer look on the force per

width change and potential evolution. The blue dotted line represented the potential evolution on the working electrode which is the Cu_2O coated ITO-glass sample and green solid line represented the force per width change on the sample surface. In figure 3.7 (b), it depicted the potential evolution occurred rapidly in the first few seconds and maintained at a constant rate of -0.25 V throughout the remaining electrodeposition time. Initial rapid development of voltage is the amount of electromotive force required to drive the current to transfer between WE and CE. The force per width change indicated compressive stress development on the sample surface upon electrodeposition process began in the first minute and stabilized for the remaining electrodeposition time. Figure 3.8 (b) showed the slope of force change in the first 5 minutes which indicated the force change only occurred rapidly in the first 30 seconds of the electrodeposition while the slope remained zero throughout the electrodeposition process. The deposition rate of Cu_2O is assumed to be constant with constant current density being applied. The initial high stress can only be observed near the Au-Cu_2O interface layer whereby no stress developed on the remaining Cu_2O deposited layers which known as stress free zone as shown in figure 3.9. The mismatched between the lattice of Au and Cu_2O had led to the compressive stress generation on the interface layer with Au-Cu_2O layer trying to expand.

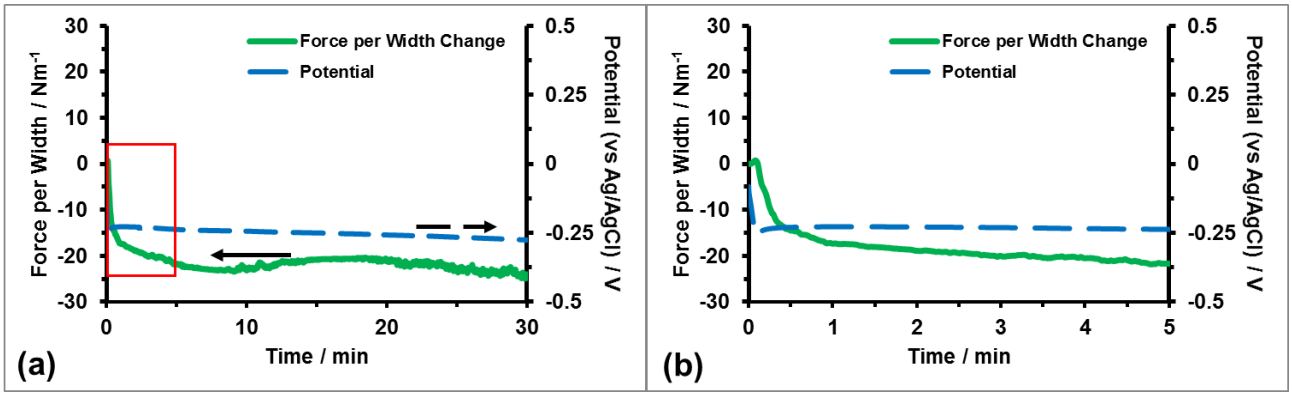

Figure 3.7. Force per width change and potential evolution during electrodeposition of Cu_2O on ITO coated glass surface at a constant current density of - 0.1 $mAcm^{-2}$ with Cu_2SO_4 aqueous solution at pH13. The blue dotted line represented the potential evolution and green solid line represented the force per width change on the sample surface. (a) Force per width change and potential evolution over 30 minutes. (b) Zoomed view of red highlighted box from (a) which show the first 5 minutes of the electrodeposition.

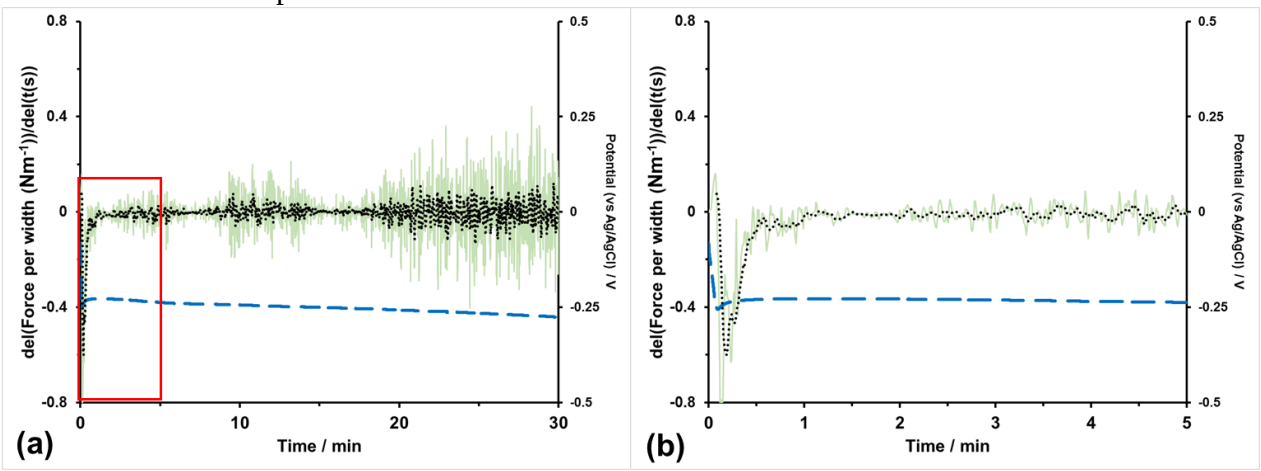

Figure 3.8 Slope of Force per width change and potential evolution during the electrodeposition of Cu_2O on ITO coated glass surface at a constant current density of - 0.1 $mAcm^{-2}$ with Cu_2SO_4 aqueous solution at pH13. Black dots correspond to the smothered version of the slope data. Dotted line corresponded to current density evolution (left aixs) while solid line corresponded to slope of force per width change (right axis). (a) Slope of Force per width change and potential evolution over 30 minutes. (b) Zoomed view of red highlighted box from (a) which show the first 5 minutes of the electrodeposition

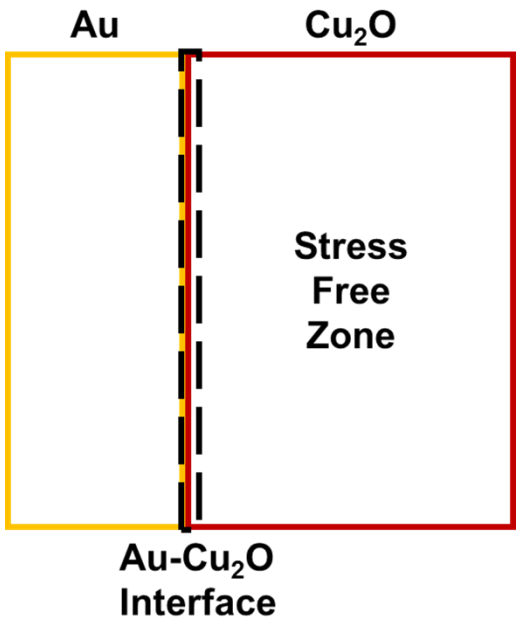

Figure 3.9 Schematic of Au and Cu_2O interface layer is the stress zone when Cu_2O is electrodeposited on the Au surface. Stress free zone located the rest of the Cu_2O deposited layer.

3.4 Conclusion

Phase shifting curvature interferometry was integrated in an electrochemical cell to enable curvature and stress change on the surface of sample during electrochemical reaction. The smallest curvature change that could be resolved using curvature interferometry was roughly within 1×10^{-4} m^{-1} and the rate of curvature change is 2.5×10^{-8} $m^{-1}s^{-1}$. Both the smallest and rate of curvature change demonstrated the ability of curvature interferometer to measure deflection and stress change reliably. The applicability of the interferometry system for electrochemical reactions has been further tested with the electrodeposition of Cu_2O. The potential evolution and stress development of the Cu_2O electrodeposition on the Au-ITO sample developed rapidly upon the initiation of current density. The measurement of the curvature and stress revealed compressive development on the surface which indicate the Au-Cu_2O interface had high stress developed while the remaining Cu_2O layers is stress free.

3.5 References

[1] Chen, Zhebo, Huyen N. Dinh, and Eric Miller. *Photoelectrochemical water splitting*. New York: Springer, 2013.

[2] O. Khaselev and J.A. Turner: A monolithic photovoltaicphotoelectrochemical device for hydrogen production via water splitting. Science 280, 425–427 (1998).

[3] E. Aharon-Shalom and A. Heller: Efficient p-InP(Rh-H alloy) and p-InP(Re-H alloy) hydrogen evolving photocathodes. J. Electrochem. Soc. 129, 2 (1982).

[4] R. Asahi, T. Morikawa, T. Ohwaki, K. Aoki, and Y. Taga: Visible-light photocatalysis in nitrogen-doped titanium oxides. Science 293, 269–271 (2001).

[5] Z. Zou, J. Ye, K. Sayama, and H. Arakawa: Direct splitting of water under visible light irradiation with an oxide semiconductor photocatalyst. Nature 414, 625–627 (2001).

[6] K. Maeda, T. Takata, M. Hara, N. Saito, Y. Inoue, H. Kobayashi, and K. Domen: GaN:ZnO solid solution as a photocatalyst for visible-light-driven overall water splitting. J. Am. Chem. Soc. 127, 8286–8287 (2005).

[7] A. Kay, I. Cesar, and M. Grätzel: New benchmark for water photooxidation by nanostructured a-Fe2O3 films. J. Am. Chem. Soc. 128, 15714–15721 (2006).

[8] S.W. Boettcher, E.L. Warren, M.C. Putnam, E.A. Santori, D. Turner-Evans, M.D. Kelzenberg, M.G. Walter, J.R. Mckone, B.S. Brunschwig, H.A. Atwater, and N.S. Lewis: Photoelectrochemical hydrogen evolution using Si microwire arrays. J. Am. Chem. Soc. 133, 1216–1219 (2011).

[9] J. Staszak-Jirkovsky, C.D. Malliakas, P.P. Lopes, N. Danilovic, S.S. Kota, K-C. Chang, B. Genorio, D. Strmcnik, V.R. Stamenkovic, M.G. Kanatzidis, and N.M. Markovic: Design of active and stable Co–Mo–Sx chalcogels as pH-universal catalysts for the hydrogen evolution reaction. Nat. Mater. 15, 197–203 (2016).

[10] L.R.L. Ting, Y. Deng, L. Ma, Y-J. Zhang, A.A. Peterson, and B.S. Yeo: Catalytic activities of sulfur atoms in amorphous molybdenum sulfide for the electrochemical hydrogen evolution reaction. ACS Catal. 6, 861–867 (2016).

[11] A. Fujishima and K. Honda: Electrochemical photolysis of water at a semiconductor electrode. Nature 238, 37 (1972).

[12] X. Li, J. Yu, J. Low, Y. Fang, J. Xiao, and X. Chen: Engineering heterogeneous semiconductors for solar water splitting. J. Mater. Chem. A 3, 2485–2534 (2015).

[13] X. Yan, L. Tian, M. He, and X. Chen: Three-dimensional crystalline/amorphous Co/Co3O4 core/shell nanosheets as efficient electrocatalysts for the hydrogen evolution reaction. Nano Lett. 15, 6015–6021 (2015).

[14] X. Li, J. Yu, and M. Jaroniec: Hierarchical photocatalysts. Chem. Soc. Rev. 45, 2603–2636 (2016).

[15] Lan, Tian, et al. "Effect of gold underlayer on copper (I) oxide photocathode performance." *Journal of Materials Research*32.9 (2017): 1656-1664.

[16] Lan, Tian, Colton Mundt, and Sonal Padalkar. "Influence of Morphology Controlled Gold Underlayer on Photoelectrochemical Water Splitting of Copper (I) Oxide As a Photocathode." *Meeting Abstracts*. No. 41. The Electrochemical Society, 2017.

[17] Paracchino, Adriana, et al. "Highly active oxide photocathode for photoelectrochemical water reduction." *Nature materials*10.6 (2011): 456.

[18] Yang, Yang, et al. "Cu 2 O/CuO bilayered composite as a high-efficiency photocathode for photoelectrochemical hydrogen evolution reaction." *Scientific reports* 6 (2016): 35158.

[19] Sullivan, Ian, Brandon Zoellner, and Paul A. Maggard. "Copper (I)-based p-type oxides for photoelectrochemical and photovoltaic solar energy conversion." *Chemistry of Materials*28.17 (2016): 5999-6016.

[20] Çapraz, Ömer Özgür, et al. "Role of oxide stress in the initial growth of self-organized porous aluminum oxide." *Electrochimica Acta* 167 (2015): 404-411.

[21] Çapraz, Ömer Özgür, Kurt R. Hebert, and Pranav Shrotriya. "In situ stress measurement during aluminum anodizing using phase-shifting curvature interferometry." *Journal of The Electrochemical Society* 160.11 (2013): D501-D506.

[22] Çapraz, Ömer Özgür, Pranav Shrotriya, and Kurt R. Hebert. "Measurement of stress changes during growth and dissolution of anodic oxide films on aluminum." *Journal of The Electrochemical Society* 161.5 (2014): D256-D262.

[23] Çapraz, Ömer Özgür, et al. "Factors controlling stress generation during the initial growth of porous anodic aluminum oxide." *Electrochimica Acta* 159 (2015): 16-22.

[24] H.A. Atwater and A. Polman: Plasmonics for improved photovoltaic devices. Nat. Mater. 9, 865 (2010).

[25] Q.D. Ou, Y.Q. Li, and J.X. Tang: Light manipulation in organic photovoltaics. Adv. Sci. 3, 1600123 (2016).

[26] Z. Tang, W. Tress, and O. Inganas: Light trapping in thin film organic solar cells. Mater. Today 17, 389–396 (2014).

[27] Y. Wang, E.W. Plummer, and K. Kempa: Foundations of plasmonics. Adv. Phys. 60, 799–898 (2011).

[28] X.M. Zhang, Y.L. Chen, R.S. Liu, and D.P. Tsai: Plasmonic photocatalysis. Rep. Prog. Phys. 76, 046401 (2013).

[29] G.M. Wang, Y.C. Ling, H.Y. Wang, X.H. Lu, and Y. Li: Chemically modified nanostructures for photoelectrochemical water splitting. J. Photochem. Photobiol., C 19, 35–51 (2014).

[30] P. Zhang, T. Wang, and J.L. Gong: Mechanistic understanding of the plasmonic enhancement for solar water splitting. Adv. Mater. 27, 5328–5342 (2015).

[31] Stoney, G. G., 1909, "The Tension of Metallic Films Deposited by Electrolysis,"Proc. R. Soc. London, Ser. A, 82, pp. 172–175.

[32] Freund, L. B., and Suresh, S., 2004, *Thin Film Materials; Stress, Defect Formation and Surface Evolution*, Cambridge University Press, Cambridge, U.K.

[33] Feng, X., Y. Huang, and A. J. Rosakis. "On the Stoney formula for a thin film/substrate system with nonuniform substrate thickness." *Journal of Applied Mechanics* 74.6 (2007): 1276-1281.

CHAPTER 4. CONCLUSION

4.1 General Conclusion

In this thesis dissertation, two projects are conducted which are in-situ stress measurement associated with the IGC of AA2024 and AA5083 and in-situ stress measurement associated with Electrodeposition of Cu_2O on ITO-Au Sample.

In Chapter 2, the dissolution process of both AA2024 and AA5083 resulted in the compressive stress development in the sample surface. The compressive stresses development is relatively low magnitude during open circuit exposure and stepping to the higher potential resulted in large dissolution current and rapid development of compressive stresses. Evidence of grain boundary dissolution and pits formation on surface of AA2024 and sensitized AA5083 are observed from the microstructural and compositional characterization of the sample surfaces. The EDS analysis at 5000x magnification indicated that both AA2024 and AA5083 grain boundaries show higher concentration of oxygen element which relate to the formation of oxides during the anodic dissolution. Dissolution of intermetallic particles segregated at the grain boundary results in formation of oxides associated with the volume expansion that acts as wedges in the grain boundary resulting in compressive stresses on the sample surface. The oxide formation induced wedging stresses may drive the opening of grain boundary leading to deeper penetration and may contribute to intergranular stress corrosion cracking of these alloys.

In Chapter 3, a new in-situ high resolution curvature interferometry system was developed to measure the stress during the electrodeposition of Cu_2O on ITO-Au sample. The resolution and stability of the phase shifting curvature interferometer system could be reliably measured, indicating the applicability of the system to measure bulk samples. The

compressive stress development and potential evolution are relatively high in the initial minute of the electrodeposition and remained constant throughout the remaining electrodeposition time. The rapid development of compressive stress in early electrodeposition may be due to the mismatch of lattice between the Au and Cu_2O while the remaining Cu_2O deposited layers are in stress free zone.

4.2 Future Work

In Chapter 2, we suspected the oxide formation induced wedging stresses may drive the opening of grain boundary leading to deeper penetration and may contribute to intergranular stress corrosion cracking of these alloys. One study that can be conducted is applied external tensile stress on the AA2024 and AA5083 samples prior to testing since the criteria for SCC to occur are stress, susceptible material and specific corrosive medium. The experiment results indicated the dissolution of AA2024 and AA5083 is resulted by the formation of oxide from dissolution of secondary phase particles along the grain boundary which fulfilled the two criteria for SCC.

In Chapter 3, we managed to get some preliminary stress measurement results for the PEC water splitting experiment, but more studies have to be conducted to understand how the mechanism of the Cu_2O changes with respect to the stress change. Alternative material could replace the ITO sample to provide a better and more stable reflective surface rather than depending on deposited Au layer on ITO to provide the reflective surface.